Materials Characterization 229 (2025) 115614

Contents lists available at ScienceDirect

Materials Characterization

journal homepage: www.elsevier.com/locate/matchar

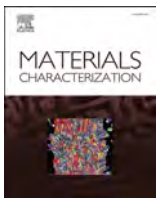

Laser powder bed fusion of copper-bearing AISI 316 L: Microstructure, biofunctional and corrosion performance

Amir Behjat [a,b], Ehsan Norouzi [c], Mahshid Kharaziha [d], Jin-Yoo Suh [c], Sara Bagherifard [e], Mahta Khorramian [a,b], Abdollah Saboori [a,b,*]

[a] Department of Management and Production Engineering, Politecnico di Torino, Corso Duca degli Abruzzi 24, 10129 Torino, Italy
[b] Integrated Additive Manufacturing Center (IAM@PoliTo), Politecnico di Torino, Corso Castelfidardo 51, 10129 Torino, Italy
[c] Center for Energy Materials Research, Korea Institute of Science and Technology (KIST), Seoul 02792, Republic of Korea
[d] Department of Materials Engineering, Isfahan University of Technology, 84156-83111 Isfahan, Iran
[e] Department of Mechanical Engineering, Politecnico di Milano, Milano, Italy

ARTICLE INFO

Keywords:
Laser powder bed fusion
In-situ alloying
Stainless steel
Electrochemical properties
Antibacterial properties
Cytocompatibility

ABSTRACT

Developing strategies to impart antibacterial properties to biomaterials while preserving cytocompatibility is essential for addressing implant-associated infections. In this study, copper-alloyed AISI 316 L stainless steel produced by laser powder bed fusion (L-PBF) was investigated as a dual-functional biomaterial with both antibacterial and cytocompatible characteristics. Unlike previous studies that mainly focus on bulk composition, this study emphasizes the role of microstructural features unique to L-PBF processing, specifically copper micro-segregation at cellular boundaries and nanoscale oxides and examines how these influence electrochemical behavior and biological responses. Electrochemical tests suggest that the AISI 316 L-Cu samples exhibit corrosion behavior comparable to that of conventional AISI 316 L. Nevertheless, the addition of Cu resulted in diminished pitting resistance, which subsequently affected the characteristics of the passive film. Importantly, AISI 316 L-Cu demonstrate significant antibacterial activity against both Gram-positive bacteria (*Staphylococcus aureus*) and Gram-negative bacteria (*Escherichia coli*). Moreover, AISI 316 L-Cu reveals in vitro bioactivity and cytocompatibility in contact with osteoblast-like MG63 cells, supporting cell proliferation and spreading. The daily release of copper ions in physiological saline solution is measured at a trace level of parts per billion (2.5 ppb/cm^2), which is considered to pose minimal risk to human health. In summary, AISI 316 L-Cu exhibited a strong capacity to enhance both antibacterial properties and cytocompatibility, suggesting a distinct advantage for its application in orthopedic settings.

1. Introduction

AISI 316 L stainless steel is widely recognized as one of the most prevalent biomaterials, primarily due to its exceptional corrosion resistance in biological environments, which is facilitated by the spontaneous development of a thin, adherent oxide surface film [1,2]. Its biocompatibility, favorable mechanical properties, and cost-effectiveness contribute to its extensive application in various medical devices, including fracture fixation systems, surgical sutures, artificial hip joints, and microvascular and neurosurgical clips [3,4]. However, stainless steel presents certain challenges, particularly in the context of inhibiting bacterial attachment, growth, and proliferation [5,6]. This issue is crucial as reducing bacteria-induced contamination and illness has become a significant concern, particularly in the biomedical industry [7,8]. In this field, bacteria pose significant risks of disease and hygiene-related complications for humans. One promising approach to address this challenge is the development of inherently antibacterial materials, including antimicrobial stainless steels [9]. A well-established method for producing bulk antimicrobial stainless steels involves alloying with biocidal elements such as copper (Cu) or silver (Ag) [10,11]. Among them, copper has garnered considerable attention due to its broad-spectrum antibacterial properties and relatively lower material cost compared to silver [12]. Copper is a significant element in metallic biomaterials, playing a crucial role in bone fracture healing, exhibiting antibacterial properties, and contributing to cardiovascular health [13,14]. Given the robust antibacterial efficacy of copper and the

* Corresponding author at: Department of Management and Production Engineering, Politecnico di Torino, Corso Duca degli Abruzzi 24, 10129 Torino, Italy.
E-mail address: abdollah.saboori@polito.it (A. Saboori).

https://doi.org/10.1016/j.matchar.2025.115614
Received 11 April 2025; Received in revised form 1 October 2025; Accepted 2 October 2025
Available online 6 October 2025

challenges associated with implant-related infections in orthopedics, there has been a growing interest in Cu-containing implantable materials. Recently, copper has been extensively utilized in the development of antibacterial materials, with several reviews addressing various forms, including Cu-containing ceramics [15,16], Cu-containing polymer composites [17,18], and Cu-containing metal alloys [19,20]. Studies have demonstrated that the incorporation of copper into alloys can impart antibacterial properties to the material [12,13,21]. The concentration of this antibacterial alloying element in stainless steel is crucial in determining its antibacterial efficacy, with higher concentrations typically correlating with enhanced antibacterial performance [14,22]. However, it is important to note that elevated levels of copper ions can inhibit growth and exhibit toxic effects on human health. Furthermore, an increased copper content may adversely affect the mechanical properties and corrosion resistance of the alloys [23,24].

Additive manufacturing (AM) represents a transformative technology, not only due to its capacity to produce components with intricate geometries, but also because it facilitates unique opportunities for controlling microstructures and designing materials [25–27]. Unlike traditional manufacturing techniques such as casting, forging, and hot rolling, AM provides enhanced degrees of freedom for tailoring the material microstructure across various length scales [28]. Among the various AM methods, laser powder bed fusion (L-PBF), commonly referred to as selective laser melting (SLM), is the most extensively utilized technique for the fabrication of stainless steels [29,30]. This preference is attributed to the relatively abundant availability of raw powders, significant design flexibility, and the potential for cost and time efficiencies. Currently, existing research on AM alloys is primarily focused on commercially available alloys. Nevertheless, exploring novel methodologies aimed at enhancing functionality and performance, and developing new alloys specifically designed for AM through the incorporation of suitable elements, represents a compelling area of inquiry [31,32].

To this aim, this study proposed and developed a novel Cu-bearing stainless steel for biomedical applications and conducted a comprehensive investigation into its microstructure, electrochemical corrosion resistance, antibacterial properties, and biocompatibility. The potential of this alloy as a new material for orthopedic implants, along with the associated antibacterial mechanisms, is thoroughly examined for the first time.

2. Materials and methods

2.1. Materials

AISI 316 L powders (Oerlikon, particle size range of 10–45 μm) were subjected to mechanical mixing with copper powders (Sandvik Osprey Ltd., 99 % purity, particle size lower than 13 μm) at a composition of 4 wt% for a duration of 16 h within a tubular mixer. The composition is detailed in Table 1. The morphology of the AISI 316 L-Cu powder mixture is illustrated in Fig. 1(a). These figures indicate that the majority of the initial powder particles display spherical geometries, accompanied by a uniform distribution of the constituent materials. Indeed, this finding corroborates that the fine copper particles were arranged as satellites surrounding the AISI 316 L particles, thereby facilitating a uniform distribution of copper within the AISI 316 L matrix following the printing process. The EDS map analysis of the blended powders revealing a uniform distribution of copper particles within the AISI 316 L matrix powder. The particle size distributions of the initial powders were evaluated utilizing an image analysis methodology. The resulting histograms are presented in Fig. 1(b). The data illustrate that the average particle size for the starting AISI 316 L and copper powders is 27 μm (d_{10} = 13 μm, d_{50} = 23 μm, d_{90} = 40 μm) and 6.3 μm (d_{10} = 3.1 μm, d_{50} = 5.3 μm, d_{90} = 13.1 μm), respectively. For electrochemical analysis and in vitro bioactivity, simulated Body Fluid (SBF) was prepared according to the protocol established by Kokubo [33]. For a cell culture study, the osteoblast-like MG63 cell-line was purchased from the National Cell Bank of Iran at the Pasteur Institute. Dulbecco's Modified Eagle Medium (DMEM), supplemented with 10 % fetal bovine serum (FBS), phosphate buffer saline (PBS), and 1 % penicillin/streptomycin were obtained from Bioidea, Iran. Dimethyl sulfoxide (DMSO), methylthiazolyldiphenyl-tetrazolium bromide (MTT), and glutaraldehyde (25 %) were purchased from Sigma. Moreover, deionized distilled water (DDW) was used in all experiments.

2.2. Preparation of L-PBF cu-bearing AISI 316 L alloys

Prior to sample preparation, the powders were pre-dried for 2 h to remove moisture content. The commercial AISI 316 substrate was prepared by sanding with 120 mesh silicon carbide paper and subsequently cleaned with ethanol. The Cu-containing stainless steel samples, measuring 10 mm in diameter and 5 mm in thickness, were produced using an L-PBF machine (Mlab-Cusing R, Concept Laser, Germany). This process was conducted in a high-purity argon gas atmosphere, utilizing a scanning speed of 500 mm/s, a laser power of 95 W, and a hatch spacing of 84 μm. The AISI 316 L alloy was produced in a cylindrical form, measuring 10 mm in diameter and 5 mm in height, utilizing consistent processing parameters, except for the addition of copper powder. Further details regarding this methodology are available in our previous publications [34–36].

2.3. Microstructural characterization

Prior to microstructural analysis, samples were sectioned along the building direction (BD) and subjected to sanding with silicon carbide (SiC) paper, progressing from 300 grit to 4000 grit. Subsequently, the samples were polished using 1 μm diamond paste and electrolytically etched in a 65 % nitric acid solution for 20 s at a voltage of 10 V. The microstructure and elemental distribution of the etched samples were examined utilizing scanning electron microscopy (SEM, Philips XL, Netherlands) equipped with an energy-dispersive X-ray spectrometer (EDS). High-angle annular dark field scanning transmission electron microscopy (HAADF-STEM), bright field (BF) imaging, and EDS analysis were employed to visualize and confirm the presence of copper. Samples intended for TEM were prepared through focused ion beam (FIB), and TEM characterization was performed using FEI-TALOS with 200 kV accelerating voltage. Additionally, for electron backscatter diffraction (EBSD) analysis, the polished samples underwent electropolishing in a 10 vol% perchloric acid electrolyte at 25 °C, with an electrolysis voltage of 40 V for 5 s. During the EBSD examination, a SEM integrated with an EBSD probe was operated at 20 kV with a scan step of 0.35 μm.

2.4. Wettability measurements

Water contact angle measurements were performed utilizing the sessile drop technique in combination with image analysis. A microsyringe was utilized to deposit approximately 10 μL of ultrapure deionized water on the surfaces of the samples. A total of five measurements were executed for each series to determine the average static contact angle at ambient temperature.

Table 1
Nominal chemical composition of the AISI 316 L-Cu powder feedstock used in this research.

Elements	Cr	Ni	Mo	Cu	C	Mn	Si	P	S	Fe
AISI 316 L-cu (wt%)	17.42	9.50	3.04	3.57	0.02	2.41	0.48	0.022	0.01	Bal.

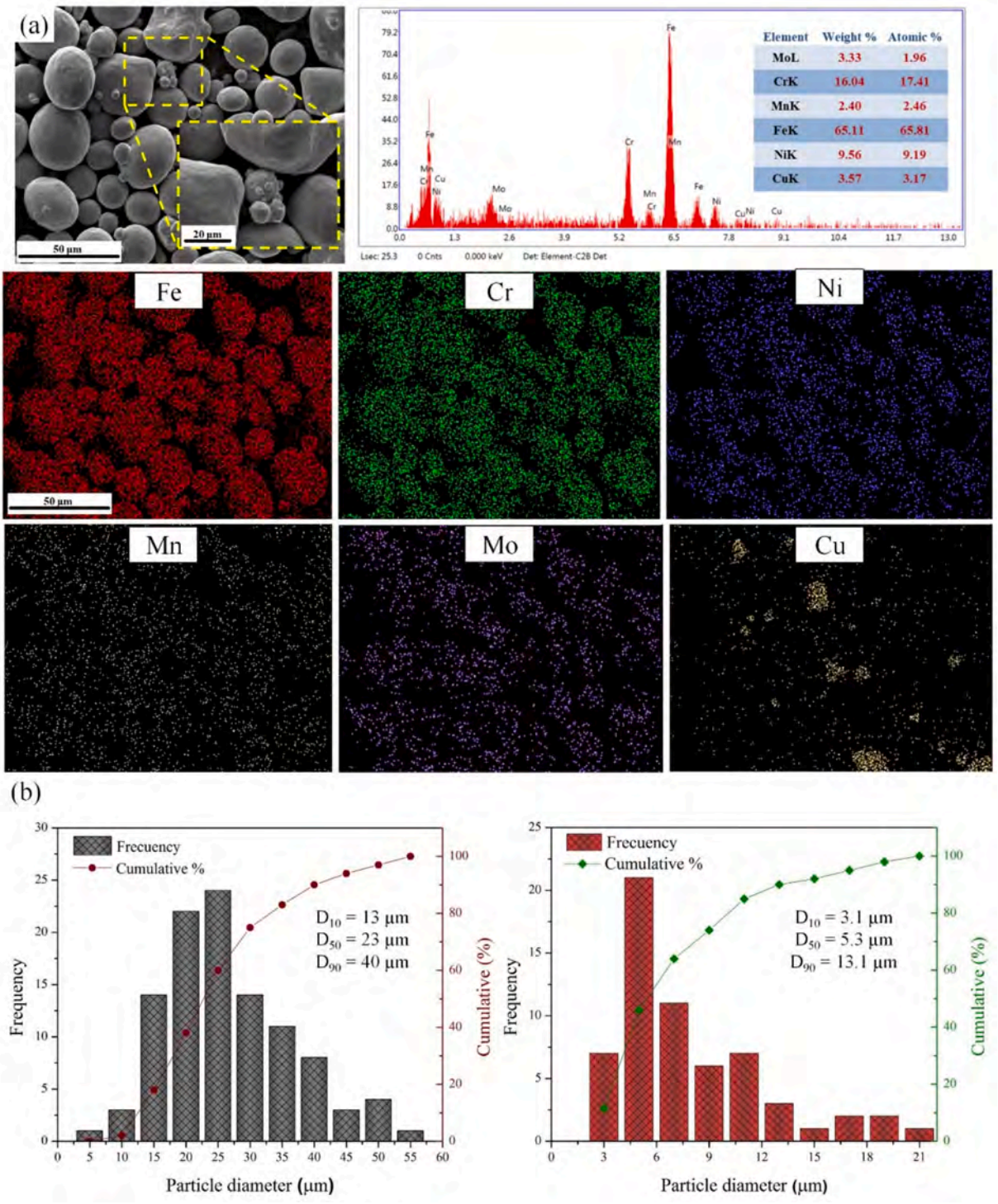

Fig. 1. (a) The morphology and high magnification of powder mixture with corresponding EDS analysis of the powders and elemental maps, and (b) particle size distributions histograms of AISI 316 L and copper powders.

2.5. X-ray photoelectron spectroscopy

An X-ray photoelectron spectrometer (XPS; FlexPS, Specs, Germany), utilizing an Al—K X-ray source with an energy of 1486.6 eV, was employed to investigate the compositional characteristics of the oxide films in the samples. High-resolution scanning was conducted for the elements iron (Fe), chromium (Cr), and copper. All spectral data were calibrated to a carbon 1 s (C 1 s) binding energy of 284.8 eV. The peak fitting analysis of the original XPS data was carried out using CasaXPS software (Version 2.3.15, USA).

2.6. Electrochemical test

Electrochemical assessments were performed utilizing an electrochemical workstation (PARASTAT 2273, Princeton Applied Research) in conjunction with a three-electrode electrolytic cell configuration. In this setup, the working electrode was represented by the sample under investigation, the reference electrode was a saturated Ag/AgCl, and the

auxiliary electrode consisted of a platinum plate. Prior to testing, the samples were prepared by grinding with silicon carbide paper to a grit size of 1200, followed by a 10-min ultrasonic cleaning in pure ethanol. Subsequently, 200 mL of SBF solution, with an initial pH of approximately 7.2, was added into the electrolytic cell, ensuring a contact area of 0.7 cm^2 between the working electrode and the solution. Prior to conducting the tests, the samples were immersed in SBF for 30 min to establish a stable open-circuit potential (OCP). Electrochemical impedance spectroscopy (EIS) measurements were performed across a frequency spectrum ranging from 10^5 Hz to 10^{-2} Hz, utilizing a perturbation signal of 10 mV. The resulting EIS data were subsequently analyzed and fitted using *Z*-View software. Cyclic potentiodynamic polarization (CPP) scans commenced at −0.25 mV relative to a saturated Ag/AgCl reference electrode, with a scanning rate of 1 mV/s. The scans were reversed upon reaching a current density of 1 mA and were terminated upon the occurrence of cathodic polarization. For the Mott–Schottky (M-S) analysis, the capacitance of the film was assessed at a frequency of 1 kHz by sweeping the applied potential in the cathodic direction from the passivation potential at a scan rate of 10 mV/s. All aforementioned electrochemical tests were conducted a minimum of three times to ensure accuracy and reliability of the results.

2.7. Copper ion concentration

The concentration of copper ions released from the AISI 316 L-Cu samples was quantified after 1, 4, and 28 days of incubation at 37 °C, utilizing an atomic absorption spectrophotometer (ICP-MS; Perkin Elmer, USA) for measurement. The AISI 316 L-Cu samples were submerged in 25 ml centrifuge tubes containing 15 ml of PBS solution at a pH of 7.4.

2.8. In vitro bioactivity evolution

The apatite-forming ability test was conducted to investigate the capacity of the alloys to facilitate apatite precipitation on their surfaces. The samples were immersed in SBF solution and maintained at 37 °C for 28 days. Subsequently, the samples were retrieved from the SBF, rinsed with distilled water, and dried in an oven. To analyze the surface morphology and composition, SEM and EDX were utilized.

2.9. Antibacterial activity

2.9.1. Plate-count method

Prior to conducting antibacterial experiments, the samples were sterilized via autoclaving for 20 min. For the antibacterial assays, 0.5 McFarland suspensions of *Escherichia coli* ATCC25922 (*E. coli*) and *Staphylococcus aureus* ATCC25923 (*S. aureus*) were prepared and subsequently diluted by a factor of 100 to reduce the concentration of colony-forming units (CFU). Then, the alloy discs were positioned at the base of a culture plate, where 20 μL of each bacterial suspension with a concentration of 10^6 CFU/mL was applied to the surface of the discs. The discs were then covered with sterilized microscopic cover glasses and incubated at 37 °C in an environment containing 5 % CO_2 and 95 % relative humidity for a duration of 24 h. Following this incubation period, each alloy disc, along with its cover glass, was transferred to a test tube containing 5 mL of PBS. The contents were mixed, and 50 μL of each resultant suspension was evenly spread onto an agar plate. The agar plates were incubated at 37 °C for 24 h, after which the colonies were enumerated. To assess the antibacterial properties of the samples, the antibacterial rate in percentage (%R) was calculated by taking the difference between the number of colonies on the control plate and the sample, and dividing it by the number of colonies in the control sample, as expressed in Eq. (1):

$$R\ (\%) = \frac{N_{control} - N_{sample}}{N_{control}} * 100 \quad (1)$$

2.9.2. Morphology of bacteria

The bacterial suspensions present on the sample surfaces were removed using a PBS solution through three wash cycles. Subsequently, the samples were subjected to a fixation process utilizing 2.5 % glutaraldehyde solution for a minimum duration of two hours. Upon completion of the fixation, the glutaraldehyde solution was eliminated, and the samples underwent a dehydration protocol involving a series of 1 mL ethanol solutions at varying concentrations (30 %, 50 %, 70 %, 90 %, and 100 %) for 20 min, aimed at immobilizing the biofilms on the sample surfaces. Following the dehydration phase, the samples were dried in an oven. Finally, an analysis of the surface morphology and bacterial distribution on the samples was performed using SEM after the application of a gold sputter coating.

2.10. Cell culture

The MG63 cell line was utilized to evaluate the cytotoxicity of the printed alloys. The cells were cultured in a humidified incubator with 5 % CO_2 at 37 °*C. prior* to cell seeding, the samples underwent sterilization by immersion in 70 % ethanol for 20 min, followed by ultraviolet (UV) irradiation on both surfaces for 4 h. After sterilization, the samples were immersed in the cell culture medium overnight. The following day, the medium was removed, and the cells were subsequently seeded onto the samples and tissue culture plate (TCP, control) at a density of 10^4 cells per sample. Subsequently, the samples were incubated, and the media was replaced every two days.

2.10.1. Cell proliferation evaluation

To assess the relative cell viability cultured on the samples, the MTT assay was performed according to the manufacturer's protocol (Sigma). Briefly, at various incubation times (1, 3, and 7 days), the medium was replaced with a fresh MTT solution (0.5 mg/mL in PBS) and incubated for 4 h to facilitate the formation of formazan crystals. Following the dissolution of formazan crystals in DMSO, the absorbance of the resultant solution was quantified using a Bio-Rad Instrument (model 680, USA) at 490 nm. The experiments were conducted for a minimum of three times, and cell viability was determined using the following Eq. (2):

$$\text{Relative cell viability} = \frac{OD\ (sample) - OD\ (blank)}{OD\ (control) - OD\ (blank)} \times 100 \quad (2)$$

where OD(sample), OD(blank), and OD(control) refer to the absorbance of the samples containing cells, DMSO, and cells without any samples.

2.10.2. Cell adhesion and morphological characterization

The morphology of cells seeded on the samples was studied using SEM. Following 1 and 7 days of culture, cells were fixed using a 2.5 % glutaraldehyde solution for 20 min and subsequently underwent dehydration in a gradient mixture of ethanol and distilled water (30, 50, 70, 90, and 95 %), with each concentration maintained for 10 min, followed by air drying. Finally, the samples were coated with a thin layer of gold and examined using SEM.

3. Results and discussion

3.1. Microstructure

Fig. 2 illustrates the EBSD results for AISI 316 L and AISI 316 L-Cu. The grain boundary coloring distribution in Fig. 2(a, d) is categorized into high angles (black colors) and low angles (green and blue colors). The results indicate that the incorporation of copper leads to a refinement of the large columnar grains in AISI 316 L, resulting in the formation of smaller columnar grains and some equiaxed grains. This modification significantly enhances the proportion of high-angle grain boundaries (HAGB), characterized by misorientation angles exceeding

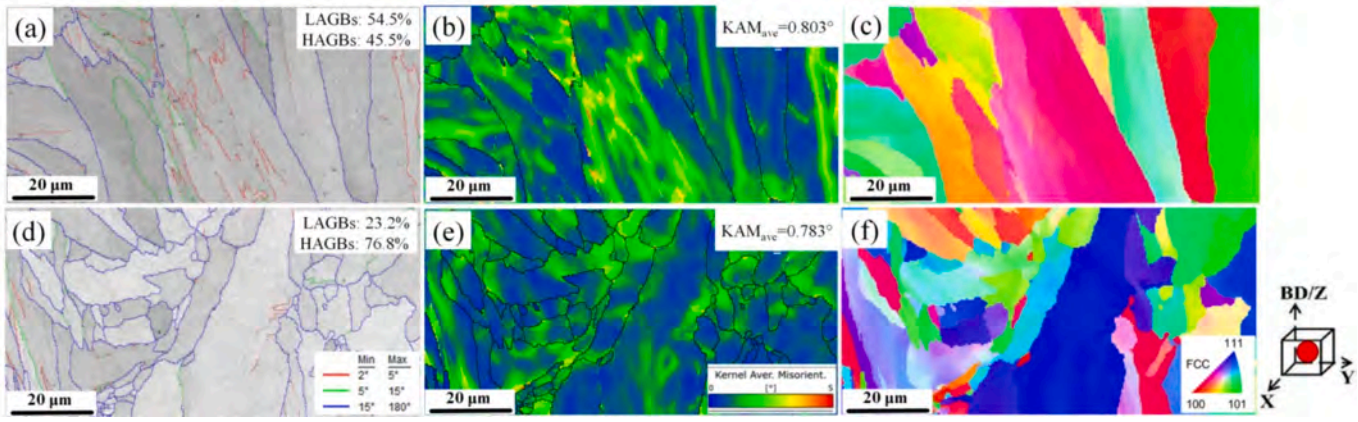

Fig. 2. Results of EBSD analysis: (a,d) Image quality with grain boundaries, (b,e) KAM results, and (c,f) IPF maps for the as-built AISI 316 L and AISI 316 L-Cu samples, respectively.

15°. The microstructural analysis of AISI 316 L-Cu reveals that the rapid solidification process effectively suppresses grain growth. The characteristics of the solidification structure are determined by the contributions of the temperature gradient (G) and the cooling rate (R) [37,38]. As the product of G and R increases, the solidification structure becomes more refined. Parameter R is influenced by various factors, including thermal conductivity and the degree of constitutional undercooling [35,36]. Copper demonstrates significantly higher thermal conductivity compared to AISI 316 L (385 W/m.K vs. 10–30 W/m.K). This enhanced thermal conductivity facilitates a higher cooling rate of the molten pool at the same laser energy. Consequently, the incorporation of copper results in an increased heat transfer rate within the molten pool, leading to a substantial degree of undercooling. This higher undercooling provides an increased driving force for the solidification process, thereby enhancing the nucleation rate and promoting grain refinement [39,40]. The resultant refined grains expand the total grain boundary area and serve as obstacles to dislocation movement.

Furthermore, copper atoms are incorporated into the metallic matrix at concentrations generally ranging from 0.5 % to 4 % by weight. The addition of copper as substitutional solute atoms within the matrix induces lattice distortions, attributable to the minor difference in atomic radii between copper and iron (0.128 nm compared to 0.126 nm) [37]. Typically, such lattice distortions inhibit dislocation movement, resulting in enhanced strength and reduced plasticity. This influence on the microstructure can be demonstrated through Kernel Average Misorientation (KAM) maps, as illustrated in the accompanying Fig. 2(b,e). The KAM maps illustrate the distribution of dislocation density, with higher KAM values generally indicating higher dislocation density [41]. This difference is not immediately apparent, as both samples exhibit a similar tendency, with KAM values predominantly located at the grain boundaries. An inverse pole figure (IPF) map, which depicts the crystallographic orientation with respect to the *Z*-axis that corresponds to the BD, was generated based on the results of the EBSD analysis, as presented in Figs. 2(c) and 2 (f). As shown, the grains in both samples predominantly exhibit a columnar structure aligned with the BD. The slight texture observed parallel to the BD is reflected in the IPF for AISI 316 L. In face-centered cubic (FCC) materials such as AISI 316 L, the preferred crystallographic growth direction for cells or dendrites is along the ⟨100⟩

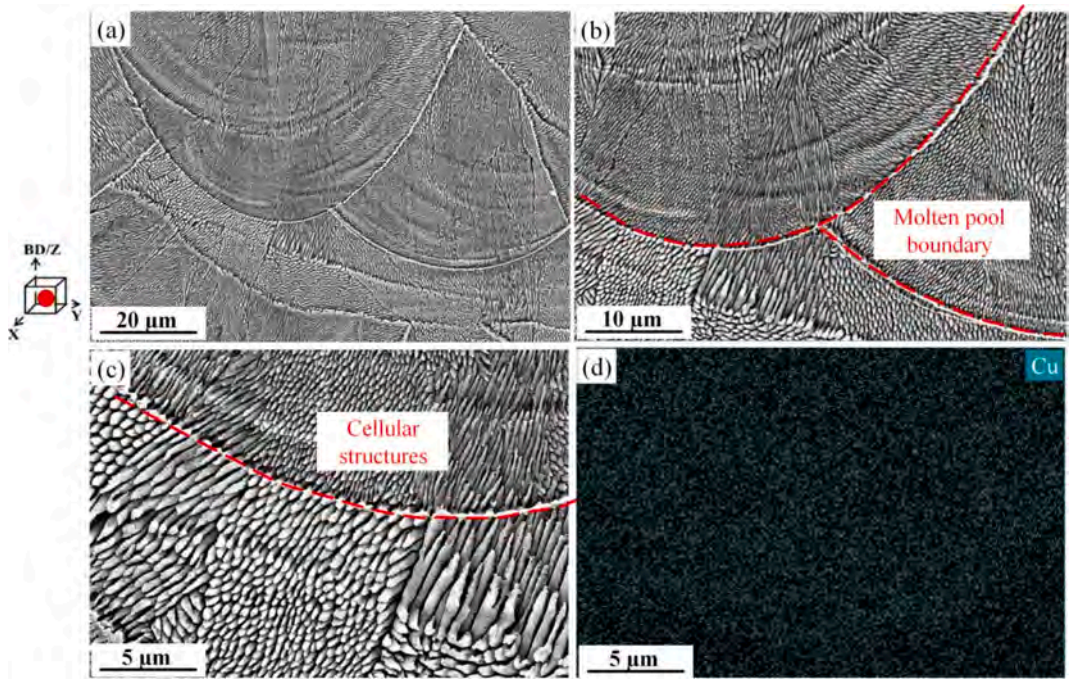

Fig. 3. (a-c) The cross-sectional SEM images of the AIS I316L-Cu and (d) the corresponding SEM-EDS copper element.

axis [42]. However, due to the curvature of the molten pool boundaries, the <100> axes of the cellular subgrains tend to deviate from the BD. Previous studies have indicated that the application of scan rotation results in the formation of a complex grain structure comprising twisted and curved grains, which are associated with an increased density of HAGBs [43,44].

The results obtained from SEM and TEM, as illustrated in Figs. (3–6), are utilized to conduct a detailed examination of the cellular structure of AISI 316 L-Cu fabricated via L-PBF. The SEM images presented in Fig. 3 (a) depict the microstructure of AISI 316 L-Cu, which typically exhibits a highly hierarchical arrangement characterized by cellular subgrains embedded within the grain structures. The inhomogeneous nucleation of grains in a new melt pool could result in multiple subgrains within a melt pool. At higher magnification, as depicted in Fig. 3(b,c), the etched microstructure reveals distinct cellular subgrain characteristics, which are commonly observed in LPBF-fabricated AISI 316 L [45,46]. Subgrains were extremely fine, approximately 0.3 to 0.8 μm in diameter. These cellular features are predominantly confined within the individual grains, exhibiting only minor local variations in orientation. The analysis does not display any significant contrast indicative of a secondary phase at this scale, aside from the presence of oxide inclusions. Furthermore, as shown in Fig. 3(d), EDS results indicate the absence of copper segregation at the austenite matrix, suggesting that copper is uniformly distributed throughout the metallic matrix, forming a solid solution during AM.

To obtain further insights into the crystallographic structure, TEM was employed. Thin foils from the cross-sectional layer (y-z plane) of LPBF- AISI 316 L-Cu were analyzed using scanning transmission electron microscopy (STEM) in dark modes to enhance the characterization of copper distributions and dislocations within the cellular structures. As illustrated in Fig. 4(a,c), the high-angle annular dark field (HAADF) images reveal a distinct bright and discontinuous boundary between the cells and their respective boundaries. Additionally, a significant presence of highly dispersed nano-oxides, represented as black circles of varying diameters, was predominantly observed at the cell boundaries and within the cells themselves.

To gain a further understanding of the elemental distribution at cellular boundaries, STEM-EDS mapping was utilized. As illustrated in Fig. 4(b), the AISI 316 L-Cu alloy exhibits a distinctive cellular structure characteristic of AISI 316 L, along with the presence of discrete copper-rich segregations at the cell boundaries, resulting from rapid solidification. No partitioning was observed in copper and molybdenum. In general, grain boundaries in polycrystalline materials can serve as pathways for the rapid diffusion of atoms, which may lead to the preferential segregation of elements at the end of the solidification process [47,48]. This phenomenon results in a more pronounced copper-rich region surrounding the subgrain boundary compared to that within the subgrain itself. Moreover, the difference between the melting point of AISI 316 L and copper (1450 °C compared to 1085 °C) could cause this phenomenon, in which copper solidifies and segregates at the cell boundaries during rapid solidification at the end of the solidification process. STEM-EDS mapping of the spherical particles as nano-sized oxides revealed a significant enrichment of manganese (Mn) and silicon (Si), as illustrated in Fig. 4(b). The chemical composition of these particles aligns with that of $MnSiO_3$ Rhodonite, which is commonly found in manganese/silicon deoxidized steels [49].

Fig. 5(a) depicts oxide particles in more detail. As shown, these particles were spherical and relatively small, measuring approximately 15 nm in size, and exhibited a uniform spatial distribution at the cell boundaries and within the cells. Several authors have demonstrated that these particles primarily originate from oxides present within the powder used during atomization. These oxides dissolve due to the high-power laser in AM, and then the rapid solidification refines the dimensions of oxide inclusions [50,51]. STEM-EDS analysis of one particular oxide in Fig. 5(b) interestingly indicated the presence of segregated copper surrounding it. This phenomenon occurred around some nano-oxide particles, which could be attributed to inhomogeneous nucleation and the accumulation of copper around them. This phenomenon may contribute to the release of copper ions, which is associated with the antibacterial effect that will be discussed in the next sections. A schematic of the mechanism that could induce micro-segregation of copper at the cell boundaries and oxide particles during solidification in L-PBF AISI 316 L-Cu alloy is shown in Fig. 5(c).

Fig. 6 displays a bright field TEM image taken along the [001] zone

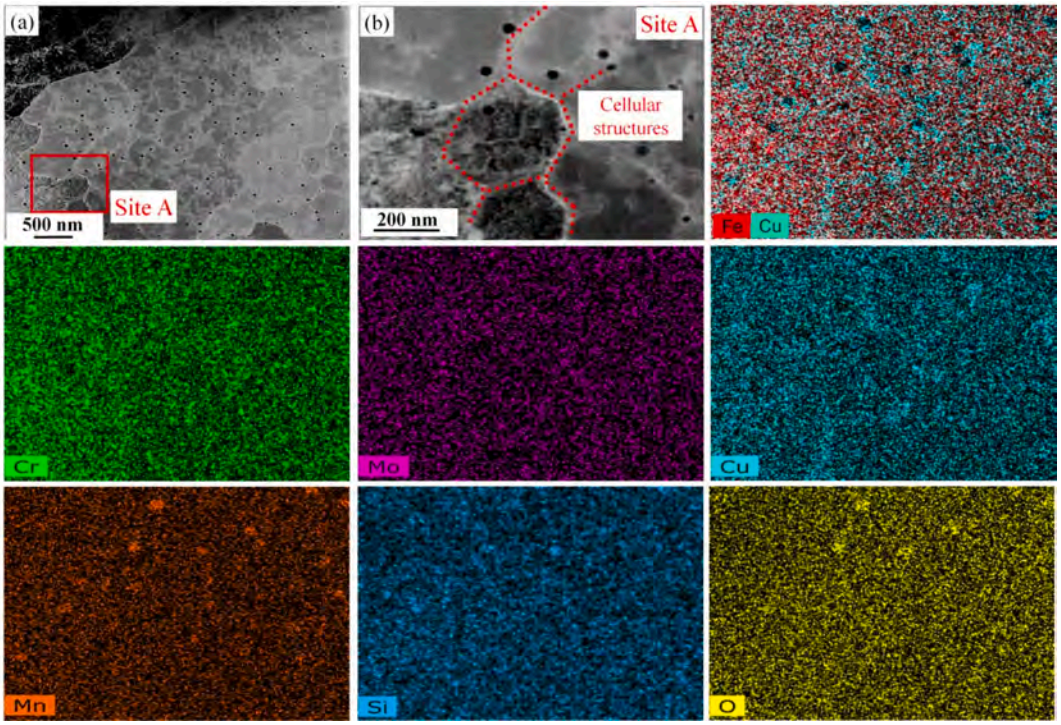

Fig. 4. (a) STEM results of AISI 316 L-Cu, (b) magnified HAADF image and corresponding STEM-EDS results of site A.

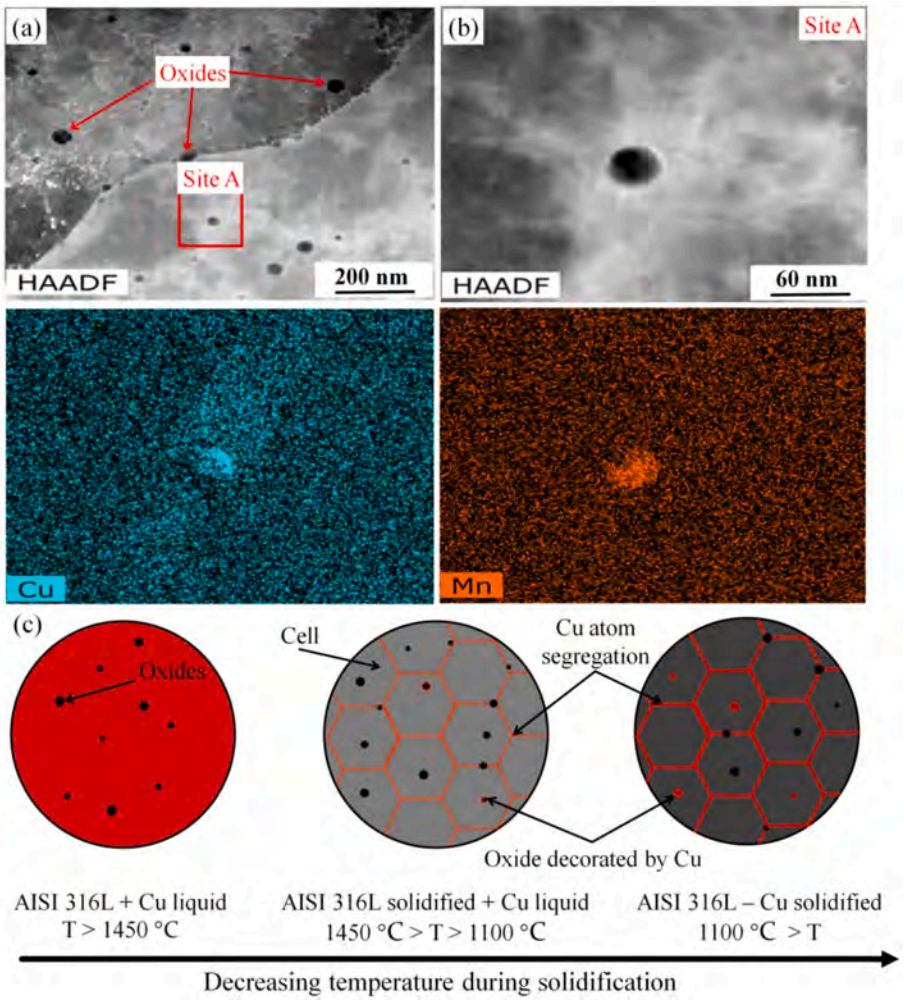

Fig. 5. (a) HAADF image of the cellular structure showing the oxides (black particles) (b) magnified HAADF image and the corresponding STEM-EDS results of site A (c) schematic of the copper segregation during solidification of L-PBF AISI 316 L-Cu.

axis, accompanied by a selected area electron diffraction (SAED) pattern. As illustrated in Fig. 6(a), the bright field mode reveals distinct cellular solidification structures characterized by a high density of dislocations at the boundaries of the cells [52–54]. Furthermore, Fig. 6(b-d) indicates that the dislocation cells present in the as-built sample consist of a complex arrangement of highly entangled dislocations. A considerable concentration of dislocations is noted within the cell structure, with a marked accumulation occurring at the cell boundaries. As illustrated in Fig. 6(e), no additional reflection spots are observable apart from the matrix, suggesting a high degree of coherency between the copper-rich regions and the austenitic matrix of AISI 316 L-Cu stainless steel. The lattice constant of the austenitic matrix closely approximates that of copper, resulting in a minimal lattice constant misfit ($\Delta\alpha/\alpha$) [55–58]. Consequently, the diffraction spots corresponding to the copper-rich regions and the matrix are challenging to differentiate due to the negligible misfit in lattice constants and atomic radii, thereby indicating a strong coherence between copper segregate regions and the austenitic matrix.

3.2. Surface characteristics

The physicochemical characteristics of interfaces, including composition, hydrophobicity, and surface charge of metallic alloys, significantly influence their corrosion and biological behavior [59,60]. In this study, the water contact angle of the alloy was analyzed to assess its wettability, as illustrated in Fig. 7(a). It is important to note that the wettability of a surface is also affected by its roughness; therefore, efforts were made to ensure that all surfaces exhibited comparable roughness after grinding. This was verified using a profilometer, which recorded a roughness value ranging from 0.9 to 1.2 μm for both alloys. The results indicate that the water contact angle for AISI 316 L-Cu was 66.5° ± 3.2°, while that for the reference AISI 316 L was 73.2° ± 2.7°. The lower contact angle indicates that the surface of the Cu-containing steel is more hydrophilic than that of the Cu-free steel.

Moreover, the corrosion resistance and biological behavior of stainless steel are profoundly influenced by the composition of the passivation film that forms on its surface [61–63]. Therefore, XPS analyses were performed to provide a more detailed understanding of the properties of this protective film. Fig. 7(b,c) displays high-resolution XPS spectra for Fe 2p, Cr 2p, and Cu 2p of the examined samples. For both samples, the Fe 2p spectra indicate the presence of iron in both the Fe^{2+} and Fe^{3+} oxidation states, which are the principal constituents of the film. The Fe^{2+} species is likely representative of FeO, whereas the Fe^{3+} species may be linked to Fe_2O_3. The Cr 2p spectra indicate the presence of Cr_2O_3, which serves as the anti-corrosive element within the film. Thus, the passive layer comprises not only Cr_2O_3 but also some oxidized iron, suggesting that iron participates in the passivation process on the surface of stainless steel, forming a mixture of oxides $(Fe/Cr)_xO_y$. This finding aligns with previous research in the field [37,64,65]. This is consistent with the Cu 2p spectra, which indicate that the binding energy of Cu 2p at 931.1 eV corresponds to Cu2O in the AISI 316 L-Cu samples. The presence of the Cu_2O characteristic peak on the surface of

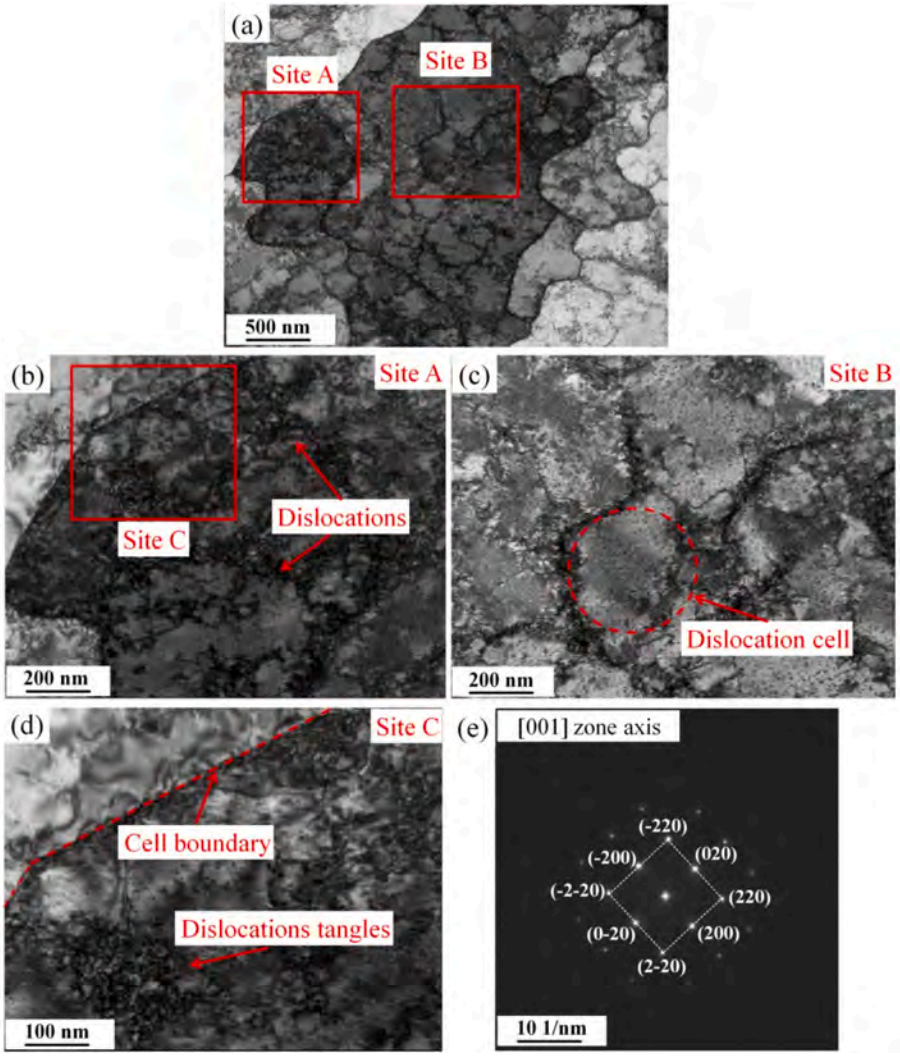

Fig. 6. (a) TEM results of the cellular structure of the AISI 316 L-Cu, (b,c) cell boundaries and dislocation structures, and (d,e) TEM image of site C and the corresponding SAED of site C.

AISI 316 L-Cu suggests that copper contributes to the formation of the passive film on this substrate. Consequently, in addition to iron and chromium, copper is also subject to oxidation, leading to the development of a thicker mixed passive film on the AISI 316 L-Cu surface. Therefore, the composition of the passive film can be represented as $(Fe/Cr/Cu)_xO_y$.

3.3. Electrochemical test and passivation film analysis

Stainless steels exhibit remarkable corrosion resistance, which is attributed to the development of a dense oxide film on their surface. Numerous studies have demonstrated that this oxide film, composed of iron and chromium oxides, effectively protects stainless steel from corrosive environments, playing a crucial role in corrosion resistance [66–68]. Fig. 8 illustrates the electrochemical findings for AISI 316 L and AISI 316 L-Cu, assessed in an SBF solution at a pH of 7.3 and a temperature of 37 °C. The relevant electrochemical parameters and the results of the fitting analyses are detailed in Tables 2 and 3.

Fig. 8(a) illustrates the variation in OCP for both alloys. The data suggest that, over time, the OCP of the samples shifts towards more positive values (anodic direction), which signifies the development of a passive film on their surface. The consistently smooth OCP curves do not exhibit any signs of metastable or active pitting corrosion. Furthermore, incorporating copper results in a shift of the equilibrium open circuit potential Eocp towards a more active state when compared to AISI 316 L.

The CPP curves for both AISI 316 L and AISI 316 L-Cu are presented in Fig. 8(b), with the direction of polarization denoted by black arrows. The electrochemical parameters, including corrosion current density (I_{corr}), passive current density (I_{pass}), and corrosion potential (E_{corr}), derived from the polarization curves are detailed in Table 2. The results indicate no significant differences in E_{corr} and I_{corr} between AISI 316 L and AISI 316 L-Cu, suggesting that the incorporation of copper into AISI 316 L does not adversely affect the uniform corrosion resistance of the alloy. However, it is noteworthy that the pitting corrosion potential (E_{pit}) of AISI 316 L-Cu is reduced to 482 ± 112 mV compared to AISI 316 L, indicating a diminished resistance to pitting corrosion attributed to the addition of copper. This aspect is particularly critical for metallic biomaterials, especially in the context of orthopedic implants, as pitting sites can serve as initiation points for cracks, thereby compromising the mechanical integrity of the implants [69,70]. Consequently, future research should focus on enhancing pitting corrosion resistance while minimizing copper ion release.

The breakdown of passivity in stainless steels is predominantly linked to the presence of defects within the passive oxide film, which are primarily attributed to microstructural imperfections in the substrate, such as porosity and chemical inhomogeneity [61,62,71]. The AISI 316 L specimen exhibits a notably extended passive behavior, as evidenced

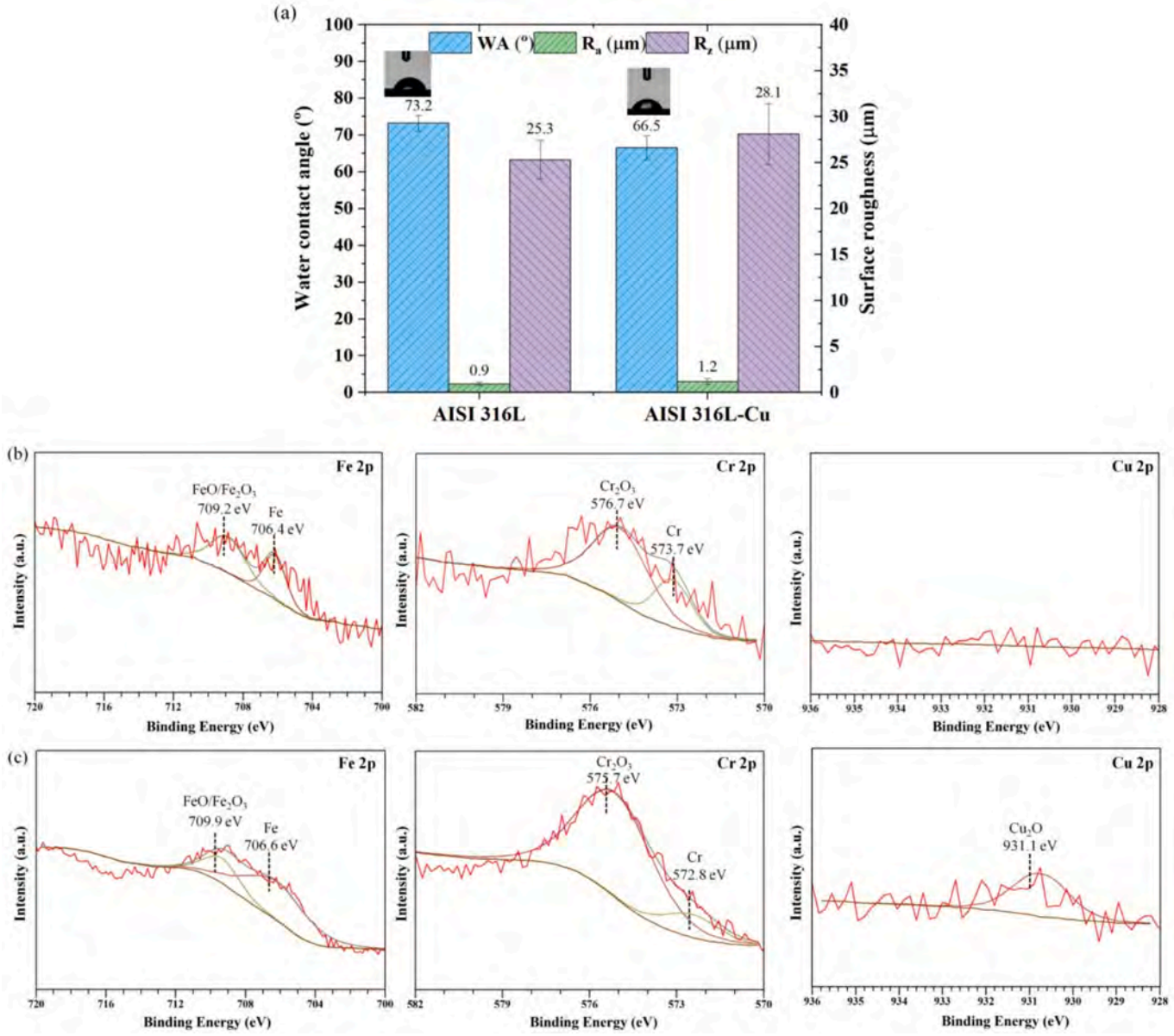

Fig. 7. (a) Variations of water contact angle and surface roughness parameters, (b,c) XPS spectra of Fe 2p, Cr 2p, and Cu 2p for AISI 316 L and AISI 316 L-Cu, respectively.

by the CPP curves (refer to Fig. 8(b)). Table 2 delineates the difference between the potential at which a marked increase in anodic current is detected as an E_{pit} and E_{corr}. These values serve to illustrate the passivity range of each specimen within the anodic polarization curves. A more extensive area of the positive hysteresis loop observed during the reverse sweep of the samples signifies a heightened susceptibility to pitting corrosion [72]. Additionally, significant variations were noted in the re-passivation characteristics of the samples. The re-passivation potential (E_{rev}) is defined as the intersection point between the reverse and forward scans. A more negative value of E_{rev} indicates a lower resistance of the material to pit propagation. Consequently, the findings suggest that the incorporation of copper into the steel matrix diminishes passivation kinetics while facilitating pit stabilization, which aligns with prior experimental findings [64,73–76]. Sourisseau et al. posited that in a neutral chloride environment, the delay in pitting repassivation induced by copper is the primary factor contributing to a reduction in pitting resistance. This implies that metallic copper hinders the formation of a passive film within an individual pit by redepositing on the pit wall, thereby obstructing the oxidation of metallic atoms, specifically iron and chromium, located beneath [74]. Furthermore, Huang et al. investigated the impact of copper distribution within microstructures, whether in solid solution or segregated into precipitates, on the corrosion resistance and antimicrobial properties of an AISI 304 L alloy containing 4 wt% copper. Their findings indicated that when copper is present in precipitate form, pitting corrosion tends to initiate from these precipitates due to their lower corrosion resistance compared to the surrounding passive layer. They concluded that, in terms of improving corrosion resistance, the retention of copper in a solid solution constitutes a more effective alloy design approach for stainless steels containing copper [75].

Following the CPP tests, the morphology of the corrosion attacks on the samples was analyzed using SEM, as shown in Fig. 9(a-d). The AISI 316 L-Cu sample exhibited significantly larger corrosion pits in comparison to the AISI 316 L material, which can be attributed to the larger positive hysteresis loop during the CPP process. EDS point analyses of the corroded AISI 316 L-copper sample revealed that the copper content in the vicinity of the pits was elevated relative to that on the surface of the samples. This copper accumulation around and within the pits may hinder the formation of a passive film and impede the repassivation

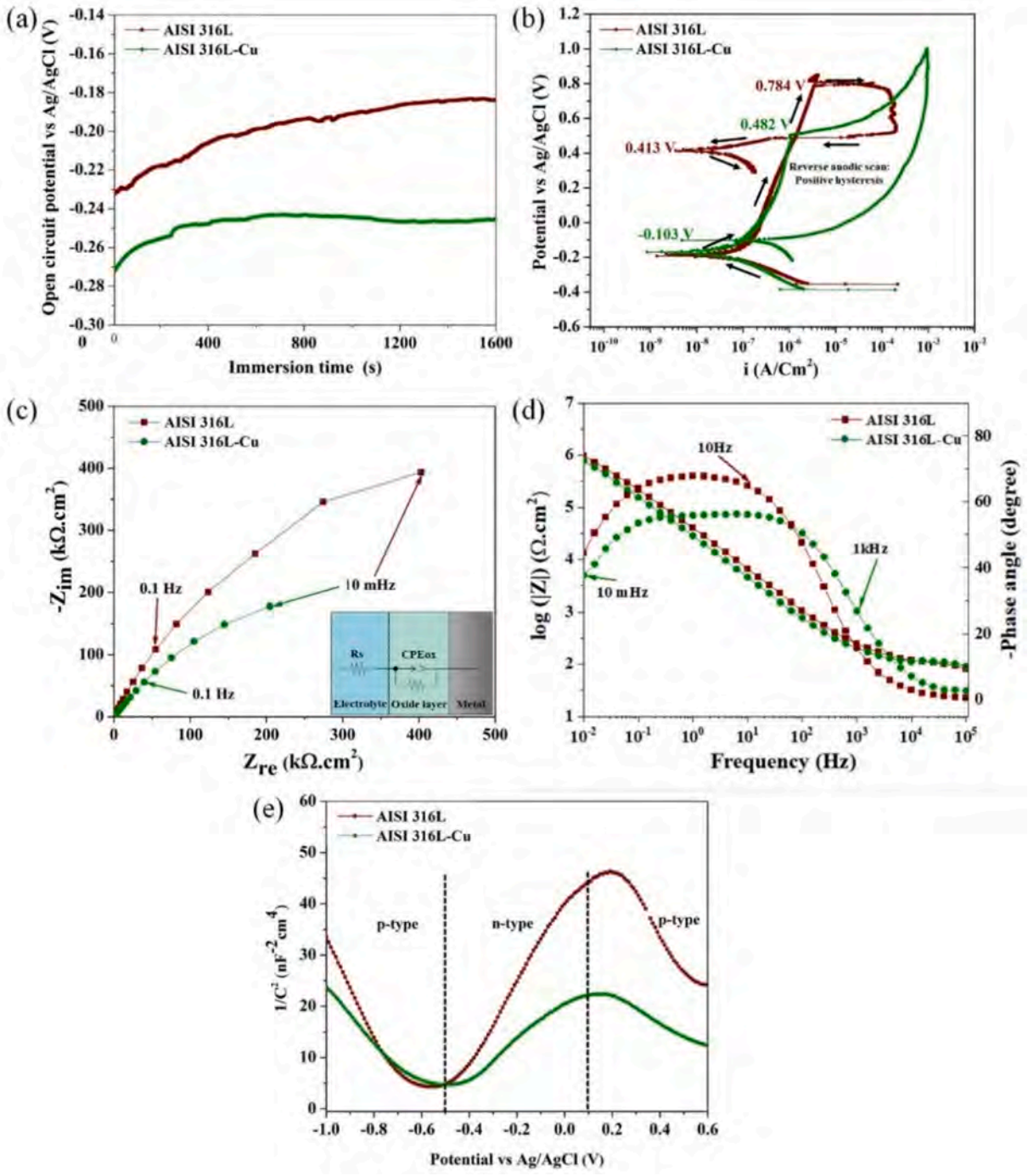

Fig. 8. Electrochemical analysis of AISI 316 L and AISI 316 L-Cu in SBF solution: (a) OCP curve, (b) CPP curve, (c) Nyquist curve and equivalent circuit, (d) Bode curve, and (e) Mott-Schottky curve.

process.

According to the above-mentioned results, Fig. 9(e) sums up the mechanism of action of copper on pitting corrosion observed on L-PBF AISI 316 L-Cu in SBF solution. In the initial stage, immediately following the commencement of CPP, a layer of oxidized products primarily consisting of metallic oxides ($(Fe/Cr/Cu)_xO_y$) forms at the material surface in contact with the SBF. Concurrently, due to the potential differences among the chromium, iron, and copper elements, metal cations such as Cr^{3+}, Fe^{2+}, Fe^{3+}, and Cu^{2+} are generated. These cations migrate along the passive layer and interact with anions present in the solution, such as Cl^- and OH^- [77]. This interaction results in a diminished stability of the passive layer, leading to its thinning. In the intermediate phase, as the potential increases during CPP, the diffusion of anions towards the passive layer is enhanced, which subsequently accelerates the dissolution rate of the passivation film. Subsequently, the passivation film undergoes breakdown, leading to the initiation of pits in areas where the passive film is deficient [78,79]. In the final stages of corrosion, pits expand as the matrix dissolves, with metallic ions such as copper remaining in an active state. Following the occurrence of pitting and the reversal of current density, the potential decreases, resulting in the reduction of dissolved copper ions alongside other ions, such as iron and chromium, which subsequently adhere to the surfaces of the ion-dissolved regions, including the pits. Concurrently, cations and anions in the solution reacted to form corrosion products, and the repassivation

Table 2
Electrochemical parameters of the samples based on the CPP curve in the SBF solution.

Materials	Parameters						
	I_{corr} ($\mu A/cm^2$)	I_{pass} ($\mu A/cm^2$)	E_{corr} (V)	E_{pit} (V)	E_{rev} (V)	E_{pit}-E_{corr} (V)	E_{pit}-E_{rev} (V)
AISI 316 L	0.42 ± 0.04	5.82 ± 0.04	−0.19 ± 0.07	0.78 ± 0.09	0.41 ± 0.01	0.97 ± 0.07	0.37 ± 0.08
AISI 316 L-cu	0.57 ± 0.03	7.33 ± 0.03	−0.17 ± 0.08	0.48 ± 0.10	−0.10 ± 0.03	0.65 ± 0.02	0.58 ± 0.07

Table 3
Fitting parameters and film thickness obtained from equivalent electrical circuit fitting.

Materials	Parameters				
	Rs (Ωcm^2)	CPE ($\mu\Omega^{-1}.sn.cm^{-2}$)	n	R_f ($M\Omega cm^2$)	dfilm (nm)
AISI 316 L	79.46 ± 0.23	12.66 ± 5.41	0.93 ± 0.03	0.69 ± 0.11	1.83 ± 0.07
AISI 316 L-cu	94.34 ± 0.15	13.82 ± 6.78	0.88 ± 0.09	0.21 ± 0.14	2.87 ± 0.14

of pits occurred [62,80]. However, the redeposition of copper, whether in metallic or oxide form, in proximity to the pits impedes the formation of the passive film and obstructs repassivation by inhibiting the oxidation of chromium and iron ions within the pits [74].

To elucidate the characteristics of the formed passive layer, it is essential to analyze the alloy utilizing EIS and M-S techniques. EIS serves as a non-destructive and highly sensitive approach for acquiring insights into the properties of the surface layer and the corrosion mechanisms prevalent in a specific environment [63]. Figs. 8(c,d) illustrate the Nyquist and Bode plots. The Nyquist plots reveal a singular capacitive loop across the entire frequency spectrum for both samples, suggesting the presence of a protective surface layer. Notably, a pronounced capacitive behavior is observed from medium to low frequencies, with phase angles nearing −80°. Such elevated phase angles are characteristic of passive materials and signify the substantial stability of the generated oxide films [62,81]. These findings align with the low corrosion current densities obtained from polarization tests, as detailed in Table 2. However, a comparative analysis of the two samples indicates that AISI 316 L-Cu exhibits a smaller impedance arc diameter, |Z|, and phase angle relative to AISI 316 L. This observation suggests a decrease in the corrosion resistance and stability of the passivation film in AISI 316 L-Cu, corroborating the results obtained from the CPP assessments.

To derive the electrochemical parameters, an equivalent circuit, as illustrated in the inset of Fig. 8(c), was employed to fit the experimental results obtained from EIS. The parameters of the equivalent circuit,

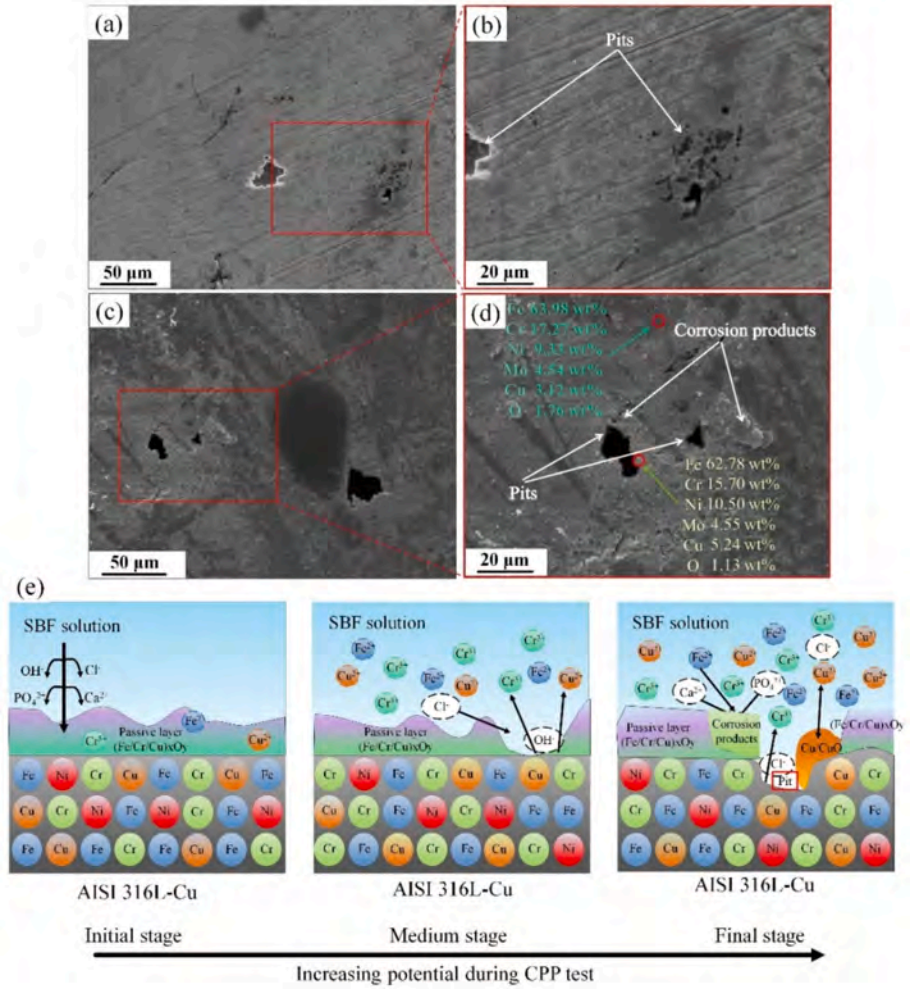

Fig. 9. SEM images of surface morphology for samples after CPP test (a,b) AISI 316 L, (c,d) AISI 316 L-Cu, and (e) Schematic illustration of corrosion mechanism proposed during CPP test for AISI 316 L-Cu.

which include solution resistance (R_s), constant phase element (*CPE*), and the resistance of the oxide film (R_f), are presented in Table 3. To account for non-ideal capacitance, the *CPE* is utilized in place of the conventional capacitance associated with the electrical double layer. The capacitive reactance can be articulated as follows (Eq. (3)) [82]:

$$Z_{CPE} = Q(\omega^{n}j)^{-1} \tag{3}$$

where Q, j, and ω represent the magnitude of the *CPE*, the imaginary unit, and the angular frequency, respectively. The Brug model was employed to determine the effective capacitance (C_{eff}) of each passive layer (Eq. (4)) [83]:

$$C_{eff} = \sqrt[n]{Q.R_T^{1-n}} \tag{4}$$

where the total resistance (R_T) is determined by the summation of the R_s and R_f. The flat region observed in the high-frequency domain of the Bode impedance plot, as illustrated in Fig. 8(d), indicates that Rs is approximately 10^4 times smaller than R_f. Consequently, the influence of R_s on the corrosion behavior of the samples is minimal and can be considered negligible. As presented in Table 3, the R_f for the AISI 316 L-Cu alloy is measured at 0.21 ± 0.14 MΩcm^2, which is roughly one-third of the value for AISI 316 L alloy (0.69 ± 0.11 MΩcm^2). A lower R_f value correlates with diminished stability of the passivation film. Therefore, it can be inferred that the incorporation of copper decreased the corrosion resistance of the original alloy. Given that the only distinction between the two stainless steel variants is the addition of copper, it is plausible that copper takes part in the formation of the oxide film on the alloy surface, which may account for the alteration in the thickness of the oxide film on the AISI 316 L-Cu alloy. The thickness of the oxide film (d_{film}) developed on the samples' surface can be calculated by Eq. (5):

$$d_{film} = \frac{\varepsilon\varepsilon 0}{C_{eff}} \tag{5}$$

where ε_0, ε, A, and C_{eff} denote the permittivity of vacuum (i.e., 8.85 × 10^{-14} F/cm), the dielectric constant of the oxide (e,g., Cr_2O_3 is 15.6 [68,81]), and the effective capacitance. The estimated thickness of the oxide film formed on the AISI 316 L and AISI 316 L-Cu samples was determined to be 1.73 ± 0.07 nm and 2.87 ± 0.14 nm, respectively. The observed increase in passive layer thickness in the presence of copper can be attributed to the enhanced dissolution rate of the AISI 316 L-Cu alloy, which facilitates the formation of more electrochemically stable corrosion products on the surface. Furthermore, the presence of copper ions within the passive film diminishes the stability of the oxide layer and increases the charge transfer flux. Indeed, the incorporation of copper not only enhances the doping level of the passivation film but also increases the propensity of the metal anode to lose electrons [37,84]. These conditions ultimately lead to an enhanced dissolution of elements, which corresponds to a decreased pitting resistance, as well as the formation of a thicker passivation layer, although this layer exhibits a lower level of corrosion resistance.

Passive oxide films formed on stainless steels display properties similar to those of highly doped semiconductors. The formation of these passive films significantly affects the chemical and electrochemical reactivity of the surface [85]. To further explore the semiconductor properties of the passivation film, the M-S curve is presented in Fig. 8(e). This analysis involved the measurement of apparent capacitance in relation to potential under depletion conditions. The Mott–Schottky equation (Eq. (6)) is expressed as follows:

$$\frac{1}{C_{SC}^{2}} = \frac{2}{e\varepsilon\varepsilon 0N}\left(E - E_{fb} - \frac{k_B T}{e}\right) \tag{6}$$

Where C_{sc} represents the capacitance of the space charge region, (e) denotes the charge of an electron (1.602 × 10^{-19}C), N refers to the density of donors (N_D) or acceptors (N_A), T indicates the absolute temperature, k_B signifies the Boltzmann constant (1.38 × 10^{-23} *J*/K), E represents the applied potential, and E_{fb} is the flatband potential, which can be ascertained through the extrapolation of C^{-2} to zero.

As depicted in Fig. 8(e), the M-S curve displays comparable characteristics, suggesting that the passive films showcase consistent electronic properties across both samples. Additionally, each plot illustrates two distinct areas that demonstrate M-S behavior, featuring linear segments with positive or negative inclinations, divided by a narrow potential plateau region. The observed positive slopes within the potential range of −0.5 to 0.1 $V_{Ag/AgCl}$ suggest that the passive film developed on both samples exhibits n-type semiconductor characteristics, as evidenced by previous studies [38,68,81]. By analyzing the linear part of the plot, it is possible to estimate the N_d using the Eq. (7):

$$Nd = \frac{2}{\varepsilon.\varepsilon 0.e.a} \tag{7}$$

where *a* is the slope in the n-type region. The N_d of the passive films was determined to be 5.67 × 10^{20} cm^{-3} for AISI 316 L and 14.78 × 10^{20} cm^{-3} for AISI 316 L-Cu. These values, which fall within the range of 10^{20} to 10^{21} cm^{-3}, are consistent with previously documented findings regarding passive films on stainless steels [65,68,81]. Notably, the N_d was generally higher for AISI 316 L-Cu, attributed to the incorporation of copper ions within the passive films. A higher N_d carrier concentration suggests an increased presence of impurity ions in the oxide film, which may compromise the stability of the passivation layer [86,87]. As previously noted in the surface analysis section, alterations in the composition of the passive film, resulting from the incorporation of additional alloying elements (or impurities) or a reduction in chromium or iron concentration, are expected to impact the electronic structure and significantly influence corrosion resistance. However, it is important to recognize that increases in N_d values do not inherently indicate the presence of impurities within the various oxides. Instead, these rises could indicate alterations in either the defect density within the space charge region or the non-stoichiometric or disordered attributes of the passive film [85,86].

The findings from the electrochemical analysis indicate that the addition of copper into AISI 316 L results in an increased defect density within the passive film, as well as a reduction in the stability of this film due to the penetration of deleterious ions, such as chloride ions (Cl^-), which arise from the dissolution of copper within the passive layer. It is important to note, however, that this particular corrosion behavior may facilitate the sustained release of copper ions, which could enhance bioactivity, a topic that will be addressed in subsequent sections.

3.4. Metal ion release

The biocompatibility of metallic biomaterials is a critical factor to consider in clinical applications, particularly for Cu-bearing materials that exhibit a certain degree of copper ion release. As a heavy metal, copper poses potential health risks to humans when its concentration exceeds a specific threshold within the body [12]. The World Health Organization (WHO) recommends an acceptable daily intake of copper ranging from 2 to 3 mg per individual [88]. To assess the release of copper from AISI 316 L-Cu during immersion testing, the quantity of copper that dissolved in PBS was measured using ICP-MS at specified intervals of 1, 7, 14, and 28 days, as illustrated in Fig. 10. The findings indicate that the daily release of copper ions was observed at trace levels, measured in parts per billion (ppb), suggesting a relatively low risk to human health. Notably, a higher release rate was recorded initially; however, it has been documented that the copper ions released during this early phase are crucial for their antibacterial properties [5,73,75]. Over time, the rate of copper ion release diminishes, which may contribute to sustained biocompatibility in the long term. Furthermore, the results demonstrate that the cumulative concentration of copper ions remains several orders of magnitude below the

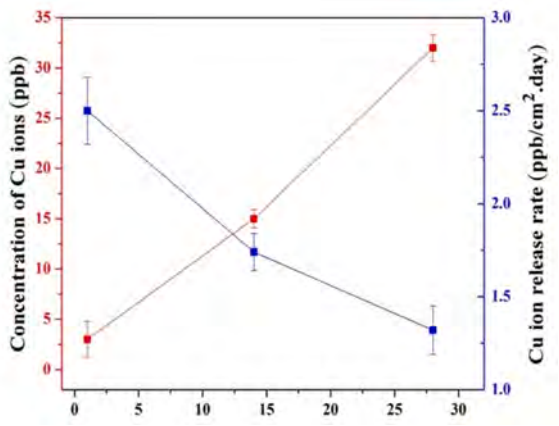

Fig. 10. Released amounts and ion release rate of copper from AISI 316 L-Cu alloy after exposure to PBS solution.

recommended daily intake, even in implants with significant surface areas. It is therefore posited that the quantity of copper ions released is unlikely to reach levels associated with symptoms of copper toxicity. Nonetheless, further long-term in vivo studies are necessary to evaluate the implications for long-lasting applications.

3.5. *In vitro bioactivity evaluation*

To investigate the potential of metallic alloys for use in implant applications, apatite-forming ability tests were conducted, and the results are presented in Fig. 11. Previous studies have demonstrated that the deposition of calcium hydroxyapatite (HA) on sample surfaces is a significant marker of their bioactivity [89,90]. The precipitation of HA was observed on the surfaces of both alloys following a 28-day incubation. The EDX analysis in Fig. 11(c,f) reveals the calcium and phosphorus content within the deposited layers. Results show that the calcium/phosphor (Ca/P) ratios of deposits on AISI 316 L and AISI 316 L-Cu were 1.35 and 1.73, respectively, which were near the natural HA ratio of 1.67 [33].

As reported, free copper ions have the potential to facilitate the differentiation of human osteoblasts, augment the biological activity of these cells, and contribute to the structural stability of the skeletal system [14,91]. Additionally, HA plays a significant role in fostering the integration of bone cells and ensuring a close association between the implant and the alveolar bone [92,93].

3.6. *Antibacterial activity evaluation*

Implant-associated infections primarily arise from adherent, sessile bacteria that establish a biofilm. Once bacteria firmly attach to a surface, they enter a protected growth state, enabling them to evade host immune responses and exhibit heightened resistance to antibiotics. It is widely recognized that the bacterial biofilm that develops on the surface of an implant is a significant contributor to infections related to surgical implants, with estimates suggesting that over 65 % of bacterial infections in humans are linked to bacterial biofilms [14,94]. The process of biofilm formation is cyclical and dynamic. Therefore, disrupting the formation of bacterial biofilms may serve as an effective strategy to mitigate the incidence of bacterial infections [95,96]. As a result, the presence of inherent strong antibacterial properties in an implant, when combined with antibiotic treatment, is anticipated to significantly diminish the likelihood of bacterial infections.

In the present study, the colony counting method was employed to assess the antibacterial properties of the alloys. The findings in Fig. 12 indicate that the AISI 316 L-Cu alloy exhibited superior antibacterial activity against both gram-positive *S. aureus* and gram-negative *E. coli* when compared to AISI 316 L. Specifically, the antibacterial efficacy of the AISI 316 L-Cu alloy was measured at 96.45 % against *E. coli* and 97.99 % against *S. aureus*, as depicted in Fig. 12(b). Given that a recommended antibacterial rate (R) of ≥90 % is considered indicative of good antibacterial properties in a material [97], it can be concluded that the synthesized AISI 316 L-Cu alloy demonstrates robust antibacterial capabilities. Previous research has demonstrated that stainless steel containing copper exhibits significant antibacterial properties attributed to the release of copper ions [12,20,73,98,99]. These ions effectively prevent the development of bacterial biofilms on the alloy's surface without causing toxicity. The release of copper ions is widely recognized as a critical player in the antimicrobial mechanism, as it is believed to inactivate bacterial cells by damaging their cell membranes and/or DNA [13,100,101]. Zhang et al. proposed that the antibacterial efficacy of Cu-bearing stainless steel is dependent on the inhibition of electron transfer within bacterial cells [101]. Conversely, the findings presented by Nan et al. provide compelling evidence that the DNA of *E. coli* did not exhibit significant damage when in contact with Cu-containing stainless steel. However, the structural integrity of the cell walls was markedly compromised, resulting in substantial leakage of cellular contents [102]. This suggests that the mechanism by which the stainless steel exerts its bactericidal effect is primarily through the disruption of the cell membrane rather than through direct damage to the DNA within the cells.

Fig. 13(a) illustrates the morphological characteristics of *S. aureus* and *E. coli* adhering to the surfaces of the material following a 24-h incubation. *E. coli* with a rod-like morphology and *S. aureus* with spherical morphology could be identified on the surface of AISI 316 L. These morphologies are similarly reported in previous studies [34,98]. Conversely, only isolated bacteria displaying shriveled or cracked morphologies were observed on the surface of AISI 316 L-Cu. The interaction between bacteria and the antibacterial AISI 316 L-Cu surface induces alterations in the structure of the bacterial outer cell membrane, resulting in compromised cell permeability. This suggests that the incorporation of copper in the developed material effectively inhibits bacterial growth and reduces adhesion on the surface of the samples.

Fig. 13(b) provides a schematic illustration that summarizes the mechanism by which the addition of copper enhances antibacterial properties. When the surface of AISI 316 L-Cu interacts with a bacterial solution, copper ions are released from the alloys via redox reactions, leading to the formation of subsequent reactions:

$$Cu \rightarrow Cu^{+} + e^{-} \quad (8)$$

$$Cu^{2+} + 2OH^{-} \rightarrow Cu_2O + 2H_2O \quad (9)$$

$$Cu^{+} + O_2 + 2H^{+} \rightarrow Cu^{2+} + H_2O_2 \quad (10)$$

In detail, the initial oxidation of copper on the material surface results in the formation of cuprous ions (Cu^{+}) (Reaction 8). It has been documented that the presence of Cu^{+} ions, which exhibit enhanced antimicrobial properties, contributes to the antimicrobial efficacy during the initial exposure period [5,13,103]. Subsequently, cuprous oxide (Cu_2O) is generated through the combined influence of chloride (Cl^{-}) and hydroxide (OH^{-}) ions (Reaction 9). However, due to the inherent instability of Cu_2O in aqueous solutions, cupric ions (Cu^{2+}) are produced under the influence of molecular oxygen (O_2) and hydrogen ions (H^{+}) (Reaction 10), leading to an overall increase in the concentration of copper in the test media [19,104]. Concurrently, the electrons released by copper facilitate the depletion of H^{+} ions while generating reactive oxygen species (ROS) (Reaction 11,12). Furthermore, the generation of free electrons catalyzes the reduction of cupric ions to cuprous ions (Reaction 13) [100,101].

$$e^{-} + O_2 \rightarrow O_2^{-} \quad (11)$$

$$2H^{+} + O_2^{-} \rightarrow H_2O_2 \quad (12)$$

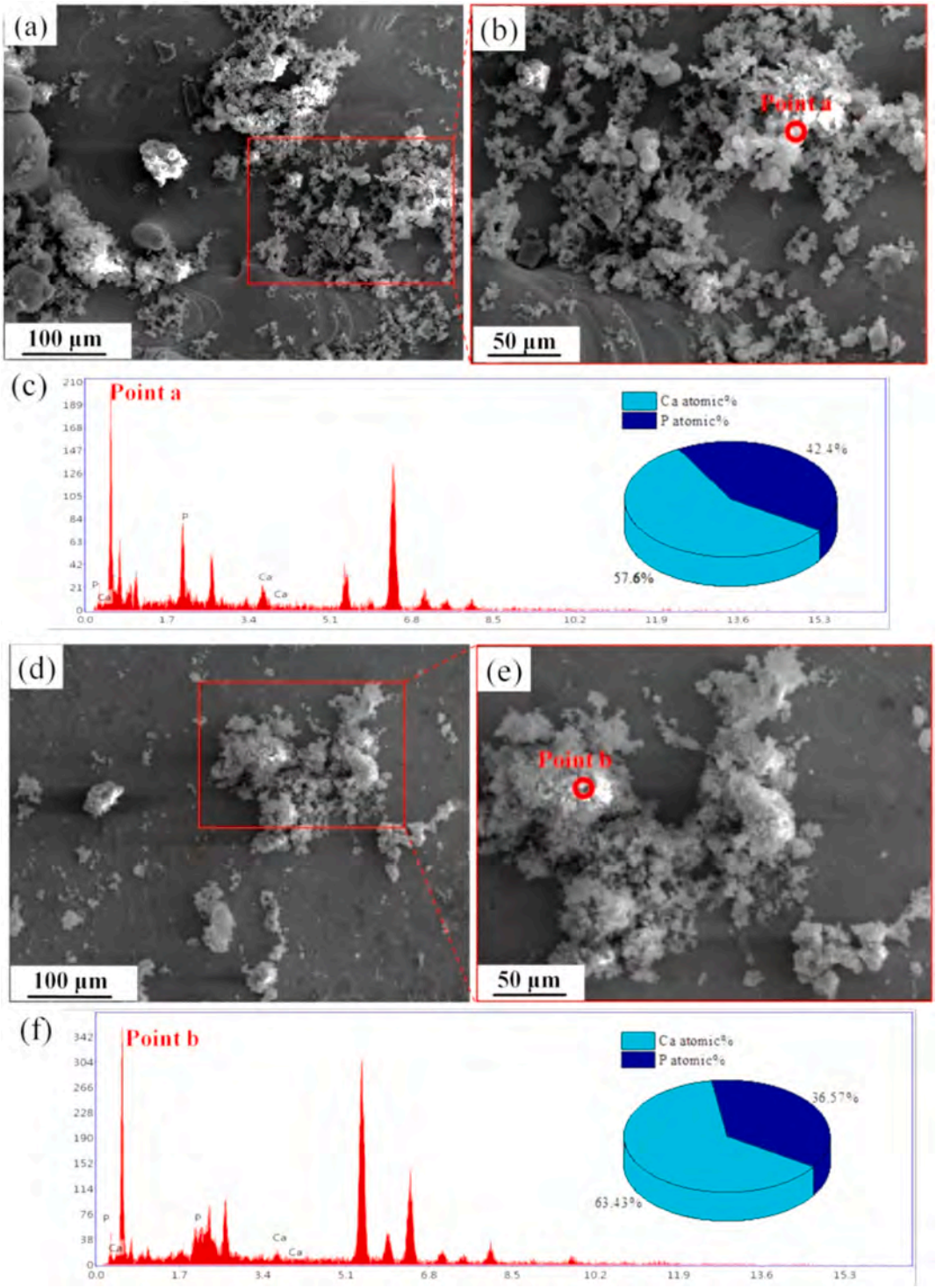

Fig. 11. SEM images and EDS spectrum of (a-c) AISI 316 L and (d-f) AISI 316 L-Cu samples after immersion in SBF for 28 days at 37 °C.

$$Cu^{2+} + O_2^- \rightarrow Cu^+ + O_2 \quad (13)$$

Meanwhile, as indicated in prior studies, the entry of copper ions into cells results in the formation of highly reactive hydroxyl radicals (OH') as a type of intracellular ROS [13]. In this context, the transition metal ion Cu^+ interacts with hydrogen peroxide (H_2O_2) under conditions of relatively low toxicity, leading to the generation of OH' through the Fenton reaction (14), as illustrated below:

$$Cu^+ + H_2O_2 \rightarrow Cu^{2+} + OH^- + OH^{\cdot} \quad (14)$$

Hydroxyl radicals are significant contributors to the products of the Fenton reaction, primarily due to their potent oxidative capabilities [105,106]. Given that a substantial quantity of H_2O_2 is generated during the aerobic respiration of bacteria, a considerable amount of high ROS is persistently produced via the Haber-Weiss cycle, as illustrated by the following two reactions (15–16) [107,108]:

$$OH^{\cdot} + H_2O_2 = O_2^{\cdot -} + H_2O + H^+ \quad (15)$$

$$O_2^{\cdot -} + H_2O_2 = O_2 + OH^- + OH^{\cdot} \quad (16)$$

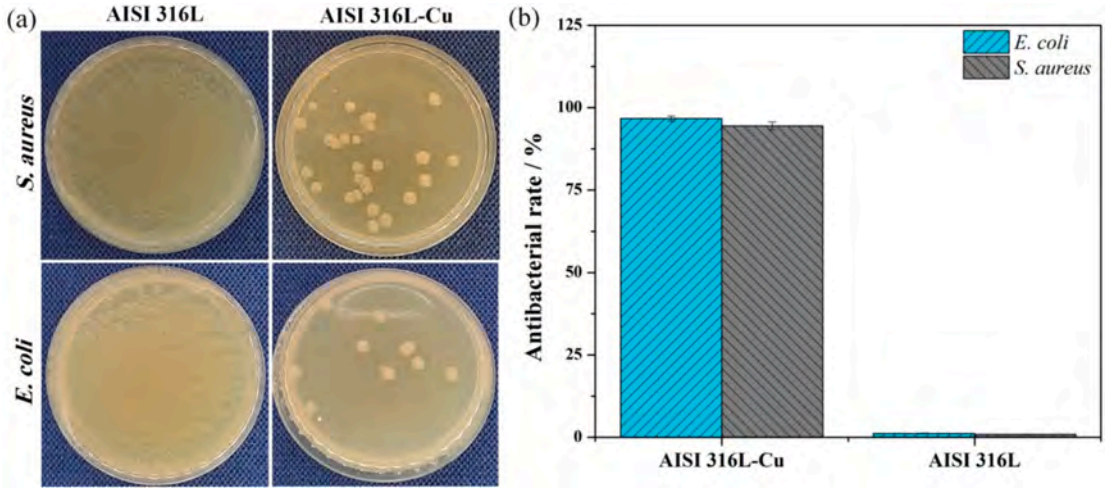

Fig. 12. (a) Typical bacteria colonies were cultured for 24 h on AISI 316 L and AISI 316 L-Cu samples, and (b) antibacterial rate of AISI 316 L and AISI 316 L-Cu.

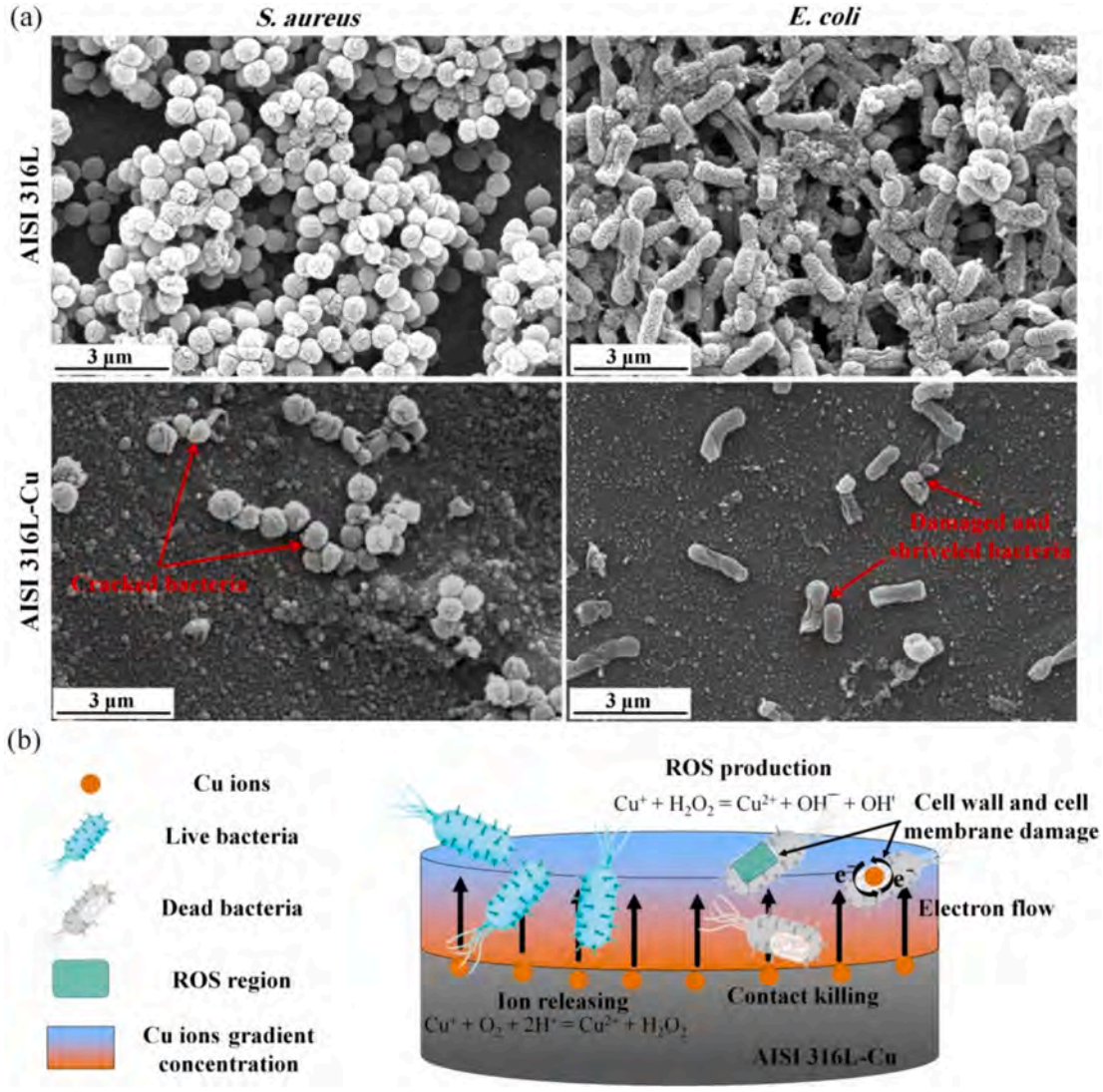

Fig. 13. (a) Surface SEM images of AISI 316 L and AISI 316 L-Cu samples against *S. aureus* and *E. coli* after incubation at 37 °C for 24 h, and (b) Schematic describing the antibacterial mechanism of AISI 316 L-Cu alloy.

The increase in high ROS is associated with heightened toxicity, which can activate receptor pathways, leading to irreversible cellular damage and potential apoptosis. Consequently, the findings suggest that higher levels of ROS correlate with an increased efficacy in contact killing. These reactive species interact with critical biological molecules, including lipids, proteins, and nucleic acids, resulting in oxidative damage or cellular death [109].

3.7. Cytocompatibility evaluation

Biosafety and favorable cytocompatibility are fundamental criteria in the development of prospective medical devices. Effective interaction between cells and implants, characterized by processes such as cell spreading, proliferation, and differentiation, is essential for the utilization of biocompatible materials [14,21,110,111]. The MTT assay was employed to evaluate cell viability and proliferation of AISI 316 L-Cu alloy in comparison to AISI 316 L. Fig. 14 presents the viability of MG63 cells seeded on the samples. The findings indicated that the number of cells adhering to the surface of the samples increased with prolonged culture time. The cell viability for both samples was recorded at less than 100 % but greater than 75 % on both the first and third days, indicating a cytotoxicity classification of Grade 1. Notably, the cell viability of the AISI 316 L-Cu sample exceeded 100 % on the seventh day, which corresponds to a Grade 0 classification. This suggests that the presence of copper positively influenced cell growth, as evidenced by the higher levels of cell viability observed in samples incubated for up to 7 days. According to established standards [108], the viability rate of cells in contact with the AISI 316 L-Cu sample falls within the zero-grade range (90–100 %) for biomaterials. Hence, it can be inferred that the addition of copper to the AISI 316 L-Cu alloy does not demonstrate cytotoxic effects on MG63 cells and is beneficial for enhancing cell proliferation and metabolic activity.

Fig. 15(a) illustrates the cell adhesion and morphology following 1 and 7 days of incubation on AISI 316 L and AISI 316 L-Cu. Generally, the results indicate that both samples exhibited cellular viability, as evidenced by cell spreading and proliferation. Nevertheless, it has been documented that, in addition to cell viability, the presence of flattened cells with prominent filopodia contributes to the enhancement of bone formation around the implant substrate [112,113].

Following 24 h of incubation, a partially cohesive cellular layer was observable on the surfaces of both series of samples. The cells exhibited a star-like morphology on both types of steel; however, the degree of cell spreading was more pronounced on AISI 316 L-Cu than on AISI 316 L. Following a 7-day incubation, the cell morphology transitioned to a flattened appearance. A distinct sheet-like spreading network of cells was observed, with a higher density of overlapping cells and increased intercellular interactions noted in both samples compared to the cells

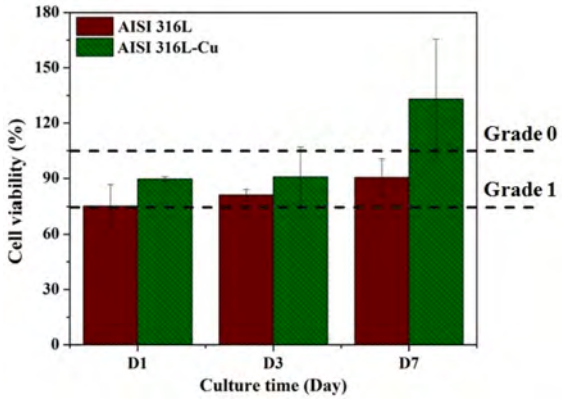

Fig. 14. Cell viability of MG63 cells in extracts of AISI 316 L and AISI 316 L-Cu alloys as a function of incubation time.

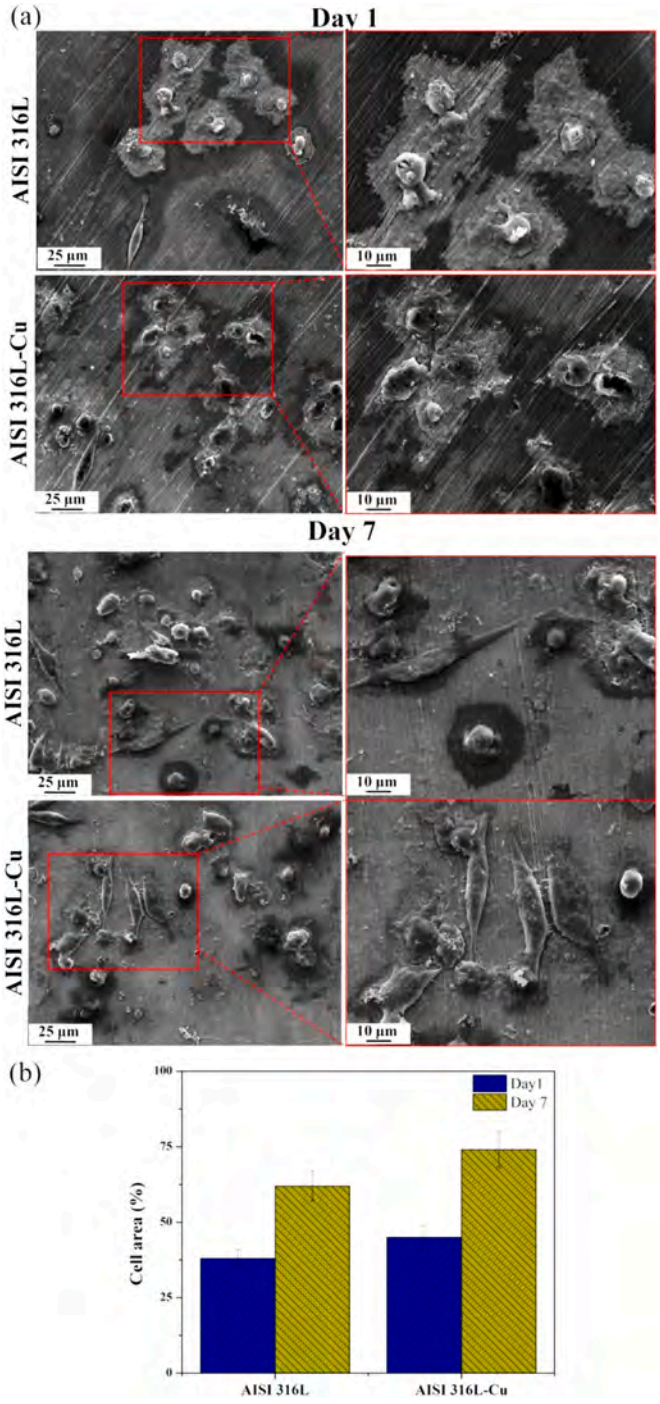

Fig. 15. MG63 cell morphology on the AISI 316 L and AISI 316 L-Cu alloys after 1 and 7 days of incubation. (a) SEM images of MG63 cells cultured, and (b) the fraction of the area of surface samples covered with MG63 cells.

incubated for 1 day. The area fraction of substrates covered by cells is presented in Fig. 15(b). A higher fraction of AISI 316 L-Cu (74 ± 6 %) compared to AISI 316 L (62 ± 5 %) was covered by cells after 7 days.

Cell proliferation and adhesion to surfaces can generally be influenced by various factors, including chemical composition, surface topology, and the rate of metallic ion release [112,114]. Given that the experiment was conducted under identical surface conditions for both samples, the effect of surface topologies can be disregarded. Consequently, the variation in the release of metallic ions from the materials may be a critical determinant of the observed differences in cell density and morphology. Therefore, in examining the distinct cytocompatibility

of AISI 316 L and AISI 316 L-Cu alloys, the impact of metallic ions on cellular metabolism and proliferation emerged as a primary focus. Copper plays a significant role in angiogenesis and osteogenesis [12,14,115]. Adequate levels of copper ions can facilitate the release of growth factors from human cells, thereby enhancing the differentiation of osteoblasts and the deposition of calcium salts [116–118]. Zhang et al. reported that the release of copper ions within the concentration range of 0.03 to 0.227 mg/L did not affect the differentiation of MG63 cells [112]. In the current investigation, the average daily concentration of copper ions released from AISI 316 L-Cu in a PBS solution was approximately 30 parts per billion (ppb), equivalent to 0.03 mg/L, as depicted in Fig. 9. This concentration is considerably lower than the maximum concentration previously documented [12].

In alignment with the findings of the present study, Gong et al. similarly reported that Cu-containing steel was beneficial for the cell attachment, viability, and proliferation of MG63 cells compared to Cu-free steel [115]. While the precise mechanisms underlying these observations require further investigation, it has been suggested that enhanced cell spreading may facilitate cell differentiation and improve cell-cell communication, which is essential for coordinating cellular behavior [116,119]. Ren et al. posited that copper ions released from Cu-bearing stainless steel promote the differentiation of osteoblasts, subsequently enhancing their growth on the material surface and ultimately leading to a more stable integration with the Cu-bearing stainless steel implant [118]. It is noteworthy that effective cell attachment and spreading on the biomaterial surface are crucial for outcompeting bacteria in the race for the surface, thereby aiding in the prevention of infection.

Overall, the findings indicate that the L-PBFed AISI 316 L-Cu exhibits dual functionality, serving as both an inductive agent for copper ions that inhibit biofilm formation and possessing robust, long-lasting antibacterial properties. Additionally, this material exhibits enhanced surface properties that are conducive to cellular functions and demonstrates favorable biocompatibility.

4. Conclusions

This article presents a comprehensive investigation into the effects of copper on the microstructure, corrosion resistance, antibacterial properties, and biocompatibility of L-PBF AISI 316 L-Cu alloy. The main conclusions are summarized as follows:

1) According to EBSD studies, the addition of copper to AISI 316 L appears to promote grain refinement and an increase in grain boundary density. Micro-segregation is observed adjacent to nano-scale oxide inclusions and at the boundaries of cellular substructures, and copper is soluble in austenite. These microstructural trends, however, need to be verified by a more thorough statistical analysis since they are based on limited EBSD data.
2) Electrochemical tests revealed that a thicker and more defective passive oxide surface film developed on AISI 316 L-Cu, which considerably weakened pitting corrosion resistance under the experimental conditions examined.
3) According to the XPS analysis, the passive film present on the surface of AISI 316 L-Cu was primarily composed of $(Fe/Cr/Cu)_xO_y$.
4) AISI 316 L-Cu releases copper ions, which play a significant role in bacterial eradication against both gram-positive and gram-negative bacteria and promote the alloy's biological functionality.
5) In vitro biocompatibility and cellular response studies revealed that AISI 316 L-Cu improves cell adhesion, viability, and proliferation compared to copper-free steel, with no significant cytotoxic effects. While these results are intriguing, further in vivo research is required to completely evaluate the material's biological performance in physiological environments

This study emphasizes that modifying the composition of AISI 316 L through selecting and adding suitable alloying elements while leveraging the benefits of AM presents significant potential for application across various sectors, including the biomedical industry.

CRediT authorship contribution statement

Amir Behjat: Writing – original draft, Visualization, Methodology, Investigation, Formal analysis, Data curation. **Ehsan Norouzi:** Writing – original draft, Visualization, Investigation, Formal analysis, Data curation. **Mahshid Kharaziha:** Writing – review & editing, Validation, Supervision, Investigation. **Jin-Yoo Suh:** Writing – review & editing, Validation, Resources. **Sara Bagherifard:** Writing – review & editing, Resources. **Mahta Khorramian:** Writing – original draft, Formal analysis, Data curation. **Abdollah Saboori:** Writing – review & editing, Validation, Supervision, Resources, Project administration, Funding acquisition, Conceptualization.

Declaration of competing interest

The authors declare that they have no known competing financial interests or personal relationships that could have appeared to influence the work reported in this paper.

Acknowledgements

This work was partially supported by the Brain Pool program funded by the Ministry of Science and ICT (MSIT) through the National Research Foundation of Korea (NRF) (RS-2024-00400145).

Data availability

Data will be made available on request.

References

[1] M.J.K. Lodhi, K.M. Deen, M.C. Greenlee-Wacker, W. Haider, Additively manufactured 316L stainless steel with improved corrosion resistance and biological response for biomedical applications, Addit. Manuf. 27 (2019) 8–19, https://doi.org/10.1016/j.addma.2019.02.005.
[2] R. Ghanavati, H. Naffakh-Moosavy, M. Moradi, E. Gadalińska, A. Saboori, Residual stresses and distortion in additively-manufactured SS316L-IN718 multi-material by laser-directed energy deposition: a validated numerical-statistical approach, J. Manuf. Process. 108 (2023) 292–309, https://doi.org/10.1016/j.jmapro.2023.11.018.
[3] E. Davoodi, H. Montazerian, A.S. Mirhakimi, M. Zhianmanesh, O. Ibhadode, S. I. Shahabad, R. Esmaeilizadeh, E. Sarikhani, S. Toorandaz, S.A. Sarabi, R. Nasiri, Y. Zhu, J. Kadkhodapour, B. Li, A. Khademhosseini, E. Toyserkani, Additively manufactured metallic biomaterials, Bioact. Mater. 15 (2022) 214–249, https://doi.org/10.1016/j.bioactmat.2021.12.027.
[4] A. Nouri, C. Wen, Stainless Steels in Orthopedics, Struct. Biomater., Elsevier, 2021, pp. 67–101, https://doi.org/10.1016/B978-0-12-818831-6.00008-2.
[5] M. Resnik, M. Benčina, E. Levičnik, N. Rawat, A. Iglič, I. Junkar, Strategies for improving antimicrobial properties of stainless steel, Materials (Basel) 13 (2020) 2944, https://doi.org/10.3390/ma13132944.
[6] S. Bagherifard, D.J. Hickey, A.C. de Luca, V.N. Malheiro, A.E. Markaki, M. Guagliano, T.J. Webster, The influence of nanostructured features on bacterial adhesion and bone cell functions on severely shot peened 316L stainless steel, Biomaterials 73 (2015) 185–197, https://doi.org/10.1016/j.biomaterials.2015.09.019.
[7] P. Makvandi, C. Wang, E.N. Zare, A. Borzacchiello, L. Niu, F.R. Tay, Metal-based nanomaterials in biomedical applications: antimicrobial activity and cytotoxicity aspects, Adv. Funct. Mater. 30 (2020), https://doi.org/10.1002/adfm.201910021.
[8] Y. Jang, W.T. Choi, C.T. Johnson, A.J. García, P.M. Singh, V. Breedveld, D. W. Hess, J.A. Champion, Inhibition of bacterial adhesion on nanotextured stainless steel 316L by electrochemical etching, ACS Biomater Sci. Eng. 4 (2018) 90–97, https://doi.org/10.1021/acsbiomaterials.7b00544.
[9] Y. Zhuang, S. Zhang, K. Yang, L. Ren, K. Dai, Antibacterial activity of copper-bearing 316L stainless steel for the prevention of implant-related infection, J. Biomed. Mater. Res. Part B Appl. Biomater. 108 (2020) 484–495, https://doi.org/10.1002/jbm.b.34405.
[10] F.G. Echeverrigaray, S. Echeverrigaray, A.P.L. Delamare, C.H. Wanke, C. A. Figueroa, I.J.R. Baumvol, C. Aguzzoli, Antibacterial properties obtained by low-energy silver implantation in stainless steel surfaces, Surf. Coat. Technol. 307 (2016) 345–351, https://doi.org/10.1016/j.surfcoat.2016.09.005.

[11] M.A. Kaplan, A.D. Gorbenko, A.Y. Ivannikov, B.B. Kartabaeva, S.V. Konushkin, K. Y. Demin, A.S. Baikin, K.V. Sergienko, E.O. Nasakina, I.O. Bannykh, I.V. Gorudko, A.G. Kolmakov, A.V. Simakin, S.V. Gudkov, A.P. Glinushkin, M.A. Sevostyanov, Investigation of antibacterial properties of corrosion-resistant 316L steel alloyed with 0.2 wt.% and 0.5 wt.% Ag, Materials (Basel) 16 (2022) 319, https://doi.org/10.3390/ma16010319.

[12] E.-L. Zhang, S. Fu, R.-X. Wang, H.-X. Li, Y. Liu, Z.-Q. Ma, G.-K. Liu, C.-S. Zhu, G.-W. Qin, D.-F. Chen, Role of cu element in biomedical metal alloy design, Rare Metals 38 (2019) 476–494, https://doi.org/10.1007/s12598-019-01245-y.

[13] P. Mahmoudi, M.R. Akbarpour, H.B. Lakeh, F. Jing, M.R. Hadidi, B. Akhavan, Antibacterial Ti–cu implants: a critical review on mechanisms of action, Mater. Today Bio. 17 (2022) 100447, https://doi.org/10.1016/j.mtbio.2022.100447.

[14] E. Zhang, X. Zhao, J. Hu, R. Wang, S. Fu, G. Qin, Antibacterial metals and alloys for potential biomedical implants, Bioact. Mater. 6 (2021) 2569–2612, https://doi.org/10.1016/j.bioactmat.2021.01.030.

[15] S. Kargozar, M. Mozafari, S. Ghodrat, E. Fiume, F. Baino, Copper-containing bioactive glasses and glass-ceramics: from tissue regeneration to cancer therapeutic strategies, Mater. Sci. Eng. C 121 (2021) 111741, https://doi.org/10.1016/j.msec.2020.111741.

[16] T.M. Gross, J. Lahiri, A. Golas, J. Luo, F. Verrier, J.L. Kurzejewski, D.E. Baker, J. Wang, P.F. Novak, M.J. Snyder, Copper-containing glass ceramic with high antimicrobial efficacy, Nat. Commun. 10 (2019) 1979, https://doi.org/10.1038/s41467-019-09946-9.

[17] S. Alsheheri, Z. Alamshany, M.Y. Abdelaal, Preparation and physicochemical studies on polymeric nanocomposites containing copper oxide nanoparticles, Des. Monomers Polym. 26 (2023) 68–76, https://doi.org/10.1080/15685551.2023.2190222.

[18] S. Tavakoli, S. Nemati, M. Kharaziha, S. Akbari-Alavijeh, Embedding CuO nanoparticles in PDMS-SiO2 coating to improve antibacterial characteristic and corrosion resistance, Colloid Interface Sci Commun 28 (2019) 20–28, https://doi.org/10.1016/j.colcom.2018.11.002.

[19] A. Behjat, S. Sanaei, M.H. Mosallanejad, M. Atapour, M. Sheikholeslam, A. Saboori, L. Iuliano, A novel titanium alloy for load-bearing biomedical implants: evaluating the antibacterial and biocompatibility of Ti536 produced via electron beam powder bed fusion additive manufacturing process, Biomater. Adv. 163 (2024) 213928.

[20] S. Liu, H. Guo, A short review of antibacterial cu-bearing stainless steel: antibacterial mechanisms, corrosion resistance, and novel preparation techniques, J. Iron Steel Res. Int. 31 (2024) 24–45, https://doi.org/10.1007/s42243-023-01029-w.

[21] P. Wang, Y. Yuan, K. Xu, H. Zhong, Y. Yang, S. Jin, K. Yang, X. Qi, Biological applications of copper-containing materials, Bioact. Mater. 6 (2021) 916–927, https://doi.org/10.1016/j.bioactmat.2020.09.017.

[22] S. Zhang, C. Yang, G. Ren, L. Ren, Study on behaviour and mechanism of cu 2+ ion release from cu bearing antibacterial stainless steel, Mater. Technol. 30 (2015) B126–B132, https://doi.org/10.1179/1753555714Y.0000000236.

[23] J. Jiang, D. Xu, T. Xi, M.B. Shahzad, M.S. Khan, J. Zhao, X. Fan, C. Yang, T. Gu, K. Yang, Effects of aging time on intergranular and pitting corrosion behavior of cu-bearing 304L stainless steel in comparison with 304L stainless steel, Corros. Sci. 113 (2016) 46–56, https://doi.org/10.1016/j.corsci.2016.10.003.

[24] B. Li, Y. Lang, H. Chen, Z. Mi, X. Sun, H. Qu, H. Feng, Z. Tian, Copper content effects on passive film of modified 00Cr20Ni18Mo6CuN super austenitic stainless steels in acidic environment, Heliyon 9 (2023) e13652, https://doi.org/10.1016/j.heliyon.2023.e13652.

[25] D. Herzog, V. Seyda, E. Wycisk, C. Emmelmann, Additive manufacturing of metals, Acta Mater. (2016), https://doi.org/10.1016/j.actamat.2016.07.019.

[26] A. Saboori, A. Aversa, G. Marchese, S. Biamino, M. Lombardi, P. Fino, Application of directed energy deposition-based additive manufacturing in repair, Appl. Sci. 9 (2019), https://doi.org/10.3390/app9163316.

[27] S.K. Moheimani, L. Iuliano, A. Saboori, The role of substrate preheating on the microstructure, roughness, and mechanical performance of AISI 316L produced by directed energy deposition additive manufacturing, Int. J. Adv. Manuf. Technol. (2022), https://doi.org/10.1007/s00170-021-08564-4.

[28] I. Aiza, C. Baldi, F.M. de la Vega, S. Sebastiani, N.E. Veronese, M. Yousefi, M. H. Mosallanejad, E. Maleki, M. Guagliano, L. Iuliano, A. Saboori, S. Bagherifard, Effects of build orientation and inclined features on physical, microstructural and mechanical properties of powder bed fusion additively manufactured metallic parts, Prog. Mater. Sci. 147 (2025) 101357, https://doi.org/10.1016/j.pmatsci.2024.101357.

[29] M. Armstrong, H. Mehrabi, N. Naveed, An overview of modern metal additive manufacturing technology, J. Manuf. Process. 84 (2022) 1001–1029, https://doi.org/10.1016/j.jmapro.2022.10.060.

[30] J.O. Milewski, Additive Manufacturing of Metals, Springer, 2017, pp. 134–157.

[31] M.H. Mosallanejad, B. Niroumand, A. Aversa, A. Saboori, In-situ alloying in laser-based additive manufacturing processes: a critical review, J. Alloys Compd. 872 (2021) 159567, https://doi.org/10.1016/j.jallcom.2021.159567.

[32] Z. Liu, Q. Zhou, X. Liang, X. Wang, G. Li, K. Vanmeensel, J. Xie, Alloy design for laser powder bed fusion additive manufacturing: a critical review, Int. J. Extrem. Manuf. 6 (2024) 022002, https://doi.org/10.1088/2631-7990/ad1657.

[33] T. Kokubo, H. Takadama, How useful is SBF in predicting in vivo bone bioactivity? Biomaterials 27 (2006) 2907–2915, https://doi.org/10.1016/j.biomaterials.2006.01.017.

[34] A. Behjat, M. Shamanian, F. Sadeghi, L. Iuliano, A. Saboori, Additive manufacturing of a novel in-situ alloyed AISI316L-cu stainless steel: microstructure and antibacterial properties, Mater. Lett. 355 (2024) 135363, https://doi.org/10.1016/j.matlet.2023.135363.

[35] A. Behjat, M. Shamanian, L. Iuliano, A. Saboori, Laser powder bed fusion in situ alloying of AISI 316L-2.5%cu alloy: microstructure and mechanical properties evolution, Prog. Addit. Manuf. (2024), https://doi.org/10.1007/s40964-023-00557-x.

[36] A. Behjat, M. Shamanian, F. Sadeghi, M.H. Mosallanejad, A. Saboori, Process-driven structural and property evolution in laser powder bed fusion of a newly developed AISI 316L stainless steel, Materials (Basel) 18 (2025) 3343, https://doi.org/10.3390/ma18143343.

[37] Y. Liu, J. Yang, H. Yang, K. Li, Y. Qiu, W. Zhang, S. Zhou, Cu-bearing 316L stainless steel coatings produced by laser melting deposition: microstructure and corrosion behavior in simulated body fluids, Surf. Coat. Technol. 428 (2021) 127868, https://doi.org/10.1016/j.surfcoat.2021.127868.

[38] H. Zhao, Y. Ding, J. Li, G. Wei, M. Zhang, Corrosion resistance of laser melting deposited cu-bearing 316L stainless steel coating in 0.5 M H 2 SO 4 solution, Mater. Chem. Phys. 291 (2022) 126572, https://doi.org/10.1016/j.matchemphys.2022.126572.

[39] V.P. Narayana Samy, M. Schäfle, F. Brasche, U. Krupp, C. Haase, Understanding the mechanism of columnar–to-equiaxed transition and grain refinement in additively manufactured steel during laser powder bed fusion, Addit. Manuf. 73 (2023) 103702, https://doi.org/10.1016/j.addma.2023.103702.

[40] M.R. Bandekhoda, M.H. Mosallanejad, M. Atapour, et al., Investigation on the potential of laser and electron beam additively manufactured Ti–6Al–4V components for orthopedic applications, Met. Mater. Int. 30 (2024) 114–126.

[41] X. Jiang, P. Du, M. Li, H.S. Lai, F. Liu, Y. Zhong, L. Zhang, Investigating effects of element composition on the microstructure and mechanical properties of three types FeCrAl alloys through small punch test, Mater. Des. 238 (2024) 112712, https://doi.org/10.1016/j.matdes.2024.112712.

[42] S.R. Narasimharaju, W. Zeng, T.L. See, Z. Zhu, P. Scott, X. Jiang, S. Lou, A comprehensive review on laser powder bed fusion of steels: processing, microstructure, defects and control methods, mechanical properties, current challenges and future trends, J. Manuf. Process. 75 (2022) 375–414, https://doi.org/10.1016/j.jmapro.2021.12.033.

[43] S. Zou, H. Xiao, F. Ye, Z. Li, W. Tang, F. Zhu, C. Chen, C. Zhu, Numerical analysis of the effect of the scan strategy on the residual stress in the multi-laser selective laser melting, Results Phys 16 (2020) 103005, https://doi.org/10.1016/j.rinp.2020.103005.

[44] A. Leicht, C.H. Yu, V. Luzin, U. Klement, E. Hryha, Effect of scan rotation on the microstructure development and mechanical properties of 316L parts produced by laser powder bed fusion, Mater. Charact. 163 (2020) 110309, https://doi.org/10.1016/j.matchar.2020.110309.

[45] M. Moyle, C. Ledermueller, Z. Zou, S. Primig, N. Haghdadi, Multi-scale characterisation of microstructure and texture of 316L stainless steel manufactured by laser powder bed fusion, Mater. Charact. 184 (2022) 111663, https://doi.org/10.1016/j.matchar.2021.111663.

[46] D. An, Y. Xiao, X. Liu, H. Zhao, X. Li, J. Chen, Formation of two distinct cellular structures in 316L stainless steel fabricated by micro-laser beam powder-bed-fusion, Mater. Res. Lett. 12 (2024) 42–49, https://doi.org/10.1080/21663831.2023.2292076.

[47] F. Abdeljawad, S.M. Foiles, Stabilization of nanocrystalline alloys via grain boundary segregation: a diffuse interface model, Acta Mater. 101 (2015) 159–171, https://doi.org/10.1016/j.actamat.2015.07.058.

[48] F. Najafkhani, S. Kheiri, B. Pourbahari, H. Mirzadeh, Recent advances in the kinetics of normal/abnormal grain growth: a review, Arch. Civ. Mech. Eng. 21 (2021) 29, https://doi.org/10.1007/s43452-021-00185-8.

[49] F. Yan, W. Xiong, E. Faierson, G.B. Olson, Characterization of nano-scale oxides in austenitic stainless steel processed by powder bed fusion, Scr. Mater. 155 (2018) 104–108, https://doi.org/10.1016/j.scriptamat.2018.06.011.

[50] D. Riabov, E. Hryha, M. Rashidi, S. Bengtsson, L. Nyborg, Effect of atomization on surface oxide composition in 316L stainless steel powders for additive manufacturing, Surf. Interface Anal. 52 (2020) 694–706, https://doi.org/10.1002/sia.6846.

[51] N. Haghdadi, M. Laleh, M. Moyle, S. Primig, Additive manufacturing of steels: a review of achievements and challenges, J. Mater. Sci. 56 (2021) 64–107, https://doi.org/10.1007/s10853-020-05109-0.

[52] Y. Hong, C. Zhou, Y. Zheng, L. Zhang, J. Zheng, The cellular boundary with high density of dislocations governed the strengthening mechanism in selective laser melted 316L stainless steel, Mater. Sci. Eng. A 799 (2021) 140279, https://doi.org/10.1016/j.msea.2020.140279.

[53] D. Kong, C. Dong, X. Ni, L. Zhang, X. Li, Cellular size dependence on the strength of additively manufactured austenitic stainless steel, Mater. Lett. 279 (2020) 128524, https://doi.org/10.1016/j.matlet.2020.128524.

[54] E. DelVecchio, T. Liu, Y.-T. Chang, Y. Nie, M. Eslami, M.A. Charpagne, Metastable cellular structures govern localized corrosion damage development in additive manufactured stainless steel, NPJ Mater. Degrad. 8 (2024) 45, https://doi.org/10.1038/s41529-024-00464-8.

[55] S. Biswal, R.K. Barik, S. Neogy, R. Tewari, A. Dutta, D. Chakrabarti, Unravelling the mechanisms of copper precipitation-induced strengthening in austenitic stainless steels: an atomistic approach, Materialia 32 (2023) 101962, https://doi.org/10.1016/j.mtla.2023.101962.

[56] J.W. Bai, P.P. Liu, Y.M. Zhu, X.M. Li, C.Y. Chi, H.Y. Yu, X.S. Xie, Q. Zhan, Coherent precipitation of copper in Super304H austenite steel, Mater. Sci. Eng. A 584 (2013) 57–62, https://doi.org/10.1016/j.msea.2013.06.082.

[57] T. Xi, M. Babar Shahzad, D. Xu, J. Zhao, C. Yang, M. Qi, K. Yang, Copper precipitation behavior and mechanical properties of cu-bearing 316L austenitic stainless steel: a comprehensive cross-correlation study, Mater. Sci. Eng. A 675 (2016) 243–252, https://doi.org/10.1016/j.msea.2016.08.058.

[58] S.-Y. Lee, J.Y. Lee, S.-I. Lee, J.-H. Shim, Atom probe tomography study of cu precipitation behavior in 22Cr-13Ni-5Mn austenitic stainless steel, Mater. Charact. 204 (2023) 113231, https://doi.org/10.1016/j.matchar.2023.113231.

[59] S. Metwally, U. Stachewicz, Surface potential and charges impact on cell responses on biomaterials interfaces for medical applications, Mater. Sci. Eng. C 104 (2019) 109883, https://doi.org/10.1016/j.msec.2019.109883.

[60] R. Thull, Physicochemical principles of tissue material interactions, Biomol. Eng. 19 (2002) 43–50, https://doi.org/10.1016/S1389-0344(02)00009-6.

[61] V.B. Vukkum, R.K. Gupta, Review on corrosion performance of laser powder-bed fusion printed 316L stainless steel: effect of processing parameters, manufacturing defects, post-processing, feedstock, and microstructure, Mater. Des. 221 (2022) 110874, https://doi.org/10.1016/j.matdes.2022.110874.

[62] M. Laleh, A.E. Hughes, W. Xu, I. Gibson, M.Y. Tan, M. Laleh, A.E. Hughes, W. Xu, I. Gibson, M.Y. Tan, A critical review of corrosion characteristics of additively manufactured stainless steels, Int. Mater. Rev. 0 (2020) 1–37, https://doi.org/10.1080/09506608.2020.1855381.

[63] G. Sander, J. Tan, P. Balan, O. Gharbi, D.R. Feenstra, L. Singer, S. Thomas, R. G. Kelly, J.R. Scully, N. Birbilis, Corrosion of additively manufactured alloys : a review, Corrosion 9312 (2018) 1318–1350.

[64] B. Li, H. Qu, Y. Lang, H. Feng, Q. Chen, H. Chen, Copper alloying content effect on pitting resistance of modified 00Cr20Ni18Mo6CuN super austenitic stainless steels, Corros. Sci. 173 (2020) 108791, https://doi.org/10.1016/j.corsci.2020.108791.

[65] T. Lai, P. Sun, H. Sun, W. Song, C. Tang, H. Zhang, M. Chen, D. Wang, Enhancing corrosion resistance and mechanical properties of laser-direct energy deposited 316 stainless steel via W addition, Corros. Sci. 231 (2024) 111960, https://doi.org/10.1016/j.corsci.2024.111960.

[66] X.X. Wei, B. Zhang, B. Wu, Y.J. Wang, X.H. Tian, L.X. Yang, E.E. Oguzie, X.L. Ma, Enhanced corrosion resistance by engineering crystallography on metals, Nat. Commun. 13 (2022) 726, https://doi.org/10.1038/s41467-022-28368-8.

[67] G. Sander, A.P. Babu, X. Gao, D. Jiang, N. Birbilis, On the effect of build orientation and residual stress on the corrosion of 316L stainless steel prepared by selective laser melting, Corros. Sci. 179 (2021), https://doi.org/10.1016/j.corsci.2020.109149.

[68] A. Behjat, M. Shamanian, A. Taherizadeh, E. Lannunziata, S. Bagherifard, E. Gadalińska, A. Saboori, L. Iuliano, Microstructure-electrochemical behavior relationship in post processed AISI316L stainless steel parts fabricated by laser powder bed fusion, J. Mater. Res. Technol. 23 (2023) 3294–3311, https://doi.org/10.1016/j.jmrt.2023.01.229.

[69] K. Shemtov-Yona, D. Rittel, An overview of the mechanical integrity of dental implants, Biomed. Res. Int. 2015 (2015) 1–11, https://doi.org/10.1155/2015/547384.

[70] A. Behvar, Y. Aghayar, M. Avateffazeli, A. Tridello, A. Benelli, D.S. Paolino, M. Mohammadi, M. Haghshenas, Synergistic impact of corrosion pitting on the rotating bending fatigue of additively manufactured 316L stainless steel: integrated experimental and modeling analyses, Int. J. Fatigue 188 (2024) 108491, https://doi.org/10.1016/j.ijfatigue.2024.108491.

[71] J.R. Scully, N. Birbilis, Corrosion of Additively Manufactured Alloys : A Review 9312, 2018, pp. 1318–1350.

[72] M. Atapour, X. Wang, K. Färnlund, I. Odnevall Wallinder, Y. Hedberg, Corrosion and metal release investigations of selective laser melted 316L stainless steel in a synthetic physiological fluid containing proteins and in diluted hydrochloric acid, Electrochim. Acta 354 (2020) 136748, https://doi.org/10.1016/j.electacta.2020.136748.

[73] T. Xi, M.B. Shahzad, D. Xu, Z. Sun, J. Zhao, C. Yang, M. Qi, K. Yang, Effect of copper addition on mechanical properties, corrosion resistance and antibacterial property of 316L stainless steel, Mater. Sci. Eng. C 71 (2017) 1079–1085, https://doi.org/10.1016/j.msec.2016.11.022.

[74] T. Sourisseau, E. Chauveau, B. Baroux, Mechanism of copper action on pitting phenomena observed on stainless steels in chloride media, Corros. Sci. 47 (2005) 1097–1117, https://doi.org/10.1016/j.corsci.2004.05.024.

[75] H. Huang, A. Juhasz, G. Brunetti, A. Roccisano, N. Stanford, Enhanced pitting resistance and antibacterial durability of cu-bearing stainless steels via tailoring cu distributions, Materialia 31 (2023) 101880, https://doi.org/10.1016/j.mtla.2023.101880.

[76] E.E. Oguzie, J. Li, Y. Liu, D. Chen, Y. Li, K. Yang, F. Wang, The effect of cu addition on the electrochemical corrosion and passivation behavior of stainless steels, Electrochim. Acta 55 (2010) 5028–5035, https://doi.org/10.1016/j.electacta.2010.04.015.

[77] A. Pardo, M.C. Merino, M. Carboneras, F. Viejo, R. Arrabal, J. Muñoz, Influence of cu and Sn content in the corrosion of AISI 304 and 316 stainless steels in H2SO4, Corros. Sci. 48 (2006) 1075–1092, https://doi.org/10.1016/j.corsci.2005.05.002.

[78] K. Morshed-Behbahani, A. Hadadzadeh, A. Nasiri, Electrochemical insight into the passivity and corrosion of 316 L stainless steel fabricated through wire arc additive manufacturing, Colloids Surfaces A Physicochem. Eng. Asp. 693 (2024) 134085, https://doi.org/10.1016/j.colsurfa.2024.134085.

[79] S. Choudhary, R.G. Kelly, N. Birbilis, On the origin of passive film breakdown and metastable pitting for stainless steel 316L, Corros. Sci. 230 (2024) 111911, https://doi.org/10.1016/j.corsci.2024.111911.

[80] H. Parangusan, J. Bhadra, N. Al-Thani, A review of passivity breakdown on metal surfaces: influence of chloride- and sulfide-ion concentrations, temperature, and pH, Emerg. Mater. 4 (2021) 1187–1203, https://doi.org/10.1007/s42247-021-00194-6.

[81] G. Sander, S. Thomas, V. Cruz, M. Jurg, N. Birbilis, X. Gao, M. Brameld, C. R. Hutchinson, On the corrosion and metastable pitting characteristics of 316L stainless steel produced by selective laser melting, J. Electrochem. Soc. 164 (2017) C250–C257, https://doi.org/10.1149/2.0551706jes.

[82] P. Córdoba-Torres, T.J. Mesquita, O. Devos, B. Tribollet, V. Roche, R.P. Nogueira, On the intrinsic coupling between constant-phase element parameters α and Q in electrochemical impedance spectroscopy, Electrochim. Acta 72 (2012) 172–178, https://doi.org/10.1016/j.electacta.2012.04.020.

[83] G.J. Brug, A.L.G. van den Eeden, M. Sluyters-Rehbach, J.H. Sluyters, The analysis of electrode impedances complicated by the presence of a constant phase element, J. Electroanal. Chem. Interfacial Electrochem. 176 (1984) 275–295, https://doi.org/10.1016/S0022-0728(84)80324-1.

[84] H.-T. Lin, W.-T. Tsai, J.-T. Lee, C.-S. Huang, The electrochemical and corrosion behavior of austenitic stainless steel containing cu, Corros. Sci. 33 (1992) 691–697, https://doi.org/10.1016/0010-938X(92)90103-A.

[85] A. Fattah-alhosseini, F. Soltani, F. Shirsalimi, B. Ezadi, N. Attarzadeh, The semiconducting properties of passive films formed on AISI 316 L and AISI 321 stainless steels: a test of the point defect model (PDM), Corros. Sci. 53 (2011) 3186–3192, https://doi.org/10.1016/j.corsci.2011.05.063.

[86] D.D. Macdonald, The history of the point defect model for the passive state: a brief review of film growth aspects, Electrochim. Acta 56 (2011) 1761–1772, https://doi.org/10.1016/j.electacta.2010.11.005.

[87] A. Behjat, A. Saboori, M. Galati, L. Iuliano, The electrochemical behaviour of Ti-48Al-2Cr-2Nb produced by electron beam powder bed fusion process, Intermetallics 175 (2024) 108472, https://doi.org/10.1016/j.intermet.2024.108472.

[88] World Health Organization, Trace Elements in Human Nutrition and Health, Organization, 1996.

[89] H. Pan, X. Zhao, B.W. Darvell, W.W. Lu, Apatite-formation ability – predictor of "bioactivity"? Acta Biomater. 6 (2010) 4181–4188, https://doi.org/10.1016/j.actbio.2010.05.013.

[90] A.A. Zadpoor, Relationship between in vitro apatite-forming ability measured using simulated body fluid and in vivo bioactivity of biomaterials, Mater. Sci. Eng. C 35 (2014) 134–143, https://doi.org/10.1016/j.msec.2013.10.026.

[91] J. Jiao, S. Zhang, X. Qu, B. Yue, Recent advances in research on antibacterial metals and alloys as implant materials, Front. Cell. Infect. Microbiol. 11 (2021), https://doi.org/10.3389/fcimb.2021.693939.

[92] I.T. Hong, C.H. Koo, Antibacterial properties, corrosion resistance and mechanical properties of cu-modified SUS 304 stainless steel, Mater. Sci. Eng. A 393 (2005) 213–222, https://doi.org/10.1016/j.msea.2004.10.032.

[93] I. Ielo, G. Calabrese, G. De Luca, S. Conoci, Recent advances in hydroxyapatite-based biocomposites for bone tissue regeneration in orthopedics, Int. J. Mol. Sci. 23 (2022) 9721, https://doi.org/10.3390/ijms23179721.

[94] L. Kadirvelu, S.S. Sivaramalingam, D. Jothivel, D.D. Chithiraiselvan, D. Karaiyagowder Govindarajan, K. Kandaswamy, A review on antimicrobial strategies in mitigating biofilm-associated infections on medical implants, Curr. Res. Microb. Sci. 6 (2024) 100231, https://doi.org/10.1016/j.crmicr.2024.100231.

[95] S. Sharma, J. Mohler, S.D. Mahajan, S.A. Schwartz, L. Bruggemann, R. Aalinkeel, Microbial biofilm: a review on formation, infection, antibiotic resistance, control measures, and innovative treatment, Microorganisms 11 (2023) 1614, https://doi.org/10.3390/microorganisms11061614.

[96] P. Li, R. Yin, J. Cheng, J. Lin, Bacterial biofilm formation on biomaterials and approaches to its treatment and prevention, Int. J. Mol. Sci. 24 (2023) 11680, https://doi.org/10.3390/ijms241411680.

[97] M. Bao, Y. Liu, X. Wang, L. Yang, S. Li, J. Ren, G. Qin, E. Zhang, Optimization of mechanical properties, biocorrosion properties and antibacterial properties of wrought Ti-3Cu alloy by heat treatment, Bioact. Mater. 3 (2018) 28–38, https://doi.org/10.1016/j.bioactmat.2018.01.004.

[98] L. Ren, K. Yang, L. Guo, H. Chai, Preliminary study of anti-infective function of a copper-bearing stainless steel, Mater. Sci. Eng. C 32 (2012) 1204–1209, https://doi.org/10.1016/j.msec.2012.03.009.

[99] D. Sun, D. Xu, C. Yang, J. Chen, M.B. Shahzad, Z. Sun, J. Zhao, T. Gu, K. Yang, G. Wang, Inhibition of *Staphylococcus aureus* biofilm by a copper-bearing 317L-cu stainless steel and its corrosion resistance, Mater. Sci. Eng. C 69 (2016) 744–750, https://doi.org/10.1016/j.msec.2016.07.050.

[100] Z. Zhang, X.-R. Zhang, T. Jin, C.-G. Yang, Y.-P. Sun, Q. Li, K. Yang, Antibacterial mechanism of cu-bearing 430 ferritic stainless steel, Rare Metals 41 (2022) 559–569, https://doi.org/10.1007/s12598-021-01751-y.

[101] X. Zhang, C. Yang, K. Yang, Contact killing of cu-bearing stainless steel based on charge transfer caused by the microdomain potential difference, ACS Appl. Mater. Interfaces 12 (2020) 361–372, https://doi.org/10.1021/acsami.9b19596.

[102] L. Nan, W. Yang, Y. Liu, H. Xu, Y. Li, M. Lu, K. Yang, Antibacterial mechanism of copper-bearing antibacterial stainless steel against *E.coli*, J. Mater. Sci. Technol. 24 (2008) 197–201.

[103] G. Grass, C. Rensing, M. Solioz, Metallic copper as an antimicrobial surface, Appl. Environ. Microbiol. 77 (2011) 1541–1547, https://doi.org/10.1128/AEM.02766-10.

[104] X. Gai, Y. Bai, S. Li, W. Hou, Y. Hao, X. Zhang, R. Yang, R.D.K. Misra, In-situ monitoring of the electrochemical behavior of cellular structured biomedical Ti-6Al-4V alloy fabricated by electron beam melting in simulated physiological fluid, Acta Biomater. 106 (2020) 387–395, https://doi.org/10.1016/j.actbio.2020.02.008.

[105] R. Ou, G. Aodeng, J. Ai, Advancements in the application of the Fenton reaction in the cancer microenvironment, Pharmaceutics 15 (2023) 2337, https://doi.org/10.3390/pharmaceutics15092337.

[106] J. Xiao, S. Guo, D. Wang, Q. An, Fenton-like reaction: recent advances and new trends, Chem. – A Eur. J. 30 (2024), https://doi.org/10.1002/chem.202304337.

[107] A. Abdal Dayem, M. Hossain, S. Lee, K. Kim, S. Saha, G.-M. Yang, H. Choi, S.-G. Cho, The role of reactive oxygen species (ROS) in the biological activities of metallic nanoparticles, Int. J. Mol. Sci. 18 (2017) 120, https://doi.org/10.3390/ijms18010120.
[108] S.I. Liochev, I. Fridovich, The Haber-Weiss cycle—70 years later: an alternative view, Redox Rep. 7 (2002) 55–57, https://doi.org/10.1179/135100002125000190.
[109] S. Mathews, M. Hans, F. Mücklich, M. Solioz, Contact killing of Bacteria on copper is suppressed if bacterial-metal contact is prevented and is induced on Iron by copper ions, Appl. Environ. Microbiol. 79 (2013) 2605–2611, https://doi.org/10.1128/AEM.03608-12.
[110] J. Yang, H. Qin, Y. Chai, P. Zhang, Y. Chen, K. Yang, M. Qin, Y. Zhang, H. Xia, L. Ren, B. Yu, Molecular mechanisms of osteogenesis and antibacterial activity of cu-bearing Ti alloy in a bone defect model with infection in vivo, J. Orthop. Transl. 27 (2021) 77–89, https://doi.org/10.1016/j.jot.2020.10.004.
[111] J. Su, Y. Song, Z. Zhu, X. Huang, J. Fan, J. Qiao, F. Mao, Cell–cell communication: new insights and clinical implications, Signal Transduct. Target. Ther. 9 (2024) 196, https://doi.org/10.1038/s41392-024-01888-z.
[112] E. Zhang, L. Zheng, J. Liu, B. Bai, C. Liu, Influence of cu content on the cell biocompatibility of Ti–cu sintered alloys, Mater. Sci. Eng. C 46 (2015) 148–157, https://doi.org/10.1016/j.msec.2014.10.021.
[113] P.K. Mattila, P. Lappalainen, Filopodia: molecular architecture and cellular functions, Nat. Rev. Mol. Cell Biol. 9 (2008) 446–454, https://doi.org/10.1038/nrm2406.
[114] S.A. Harris, R.J. Enger, L.B. Riggs, T.C. Spelsberg, Development and characterization of a conditionally immortalized human fetal osteoblastic cell line, J. Bone Miner. Res. 10 (2009) 178–186, https://doi.org/10.1002/jbmr.5650100203.
[115] N. Gong, R.D.K. Misra, Favourable modulation of osteoblast cellular activity on cu-containing austenitic stainless steel and comparison with the cu-free counterpart, Mater. Technol. 35 (2020) 411–420, https://doi.org/10.1080/10667857.2019.1690201.
[116] Z. Zhang, H. Tang, T. Du, D. Yang, The impact of copper on bone metabolism, J. Orthop. Transl. 47 (2024) 125–131, https://doi.org/10.1016/j.jot.2024.06.011.
[117] Y. Wang, W. Zhang, Q. Yao, Copper-based biomaterials for bone and cartilage tissue engineering, J. Orthop. Transl. 29 (2021) 60–71, https://doi.org/10.1016/j.jot.2021.03.003.
[118] L. Ren, H.M. Wong, C.H. Yan, K.W.K. Yeung, K. Yang, Osteogenic ability of cu-bearing stainless steel, J. Biomed. Mater. Res. Part B Appl. Biomater. 103 (2015) 1433–1444, https://doi.org/10.1002/jbm.b.33318.
[119] L. Wang, G. Li, L. Ren, X. Kong, Y. Wang, X. Han, W. Jiang, K. Dai, K. Yang, Y. Hao, Nano-copper-bearing stainless steel promotes fracture healing by accelerating the callus evolution process, Int. J. Nanomedicine 12 (2017) 8443–8457, https://doi.org/10.2147/IJN.S146866.